



**HAL**  
open science

## Properties of the brightest young stellar clumps in extremely lensed galaxies at redshifts 4 to 5

Matteo Messa, Miroslava Dessauges-Zavadsky, Angela Adamo, Johan Richard, Adélaïde Claeysens

► **To cite this version:**

Matteo Messa, Miroslava Dessauges-Zavadsky, Angela Adamo, Johan Richard, Adélaïde Claeysens. Properties of the brightest young stellar clumps in extremely lensed galaxies at redshifts 4 to 5. Monthly Notices of the Royal Astronomical Society, 2024, 529 (3), pp.2162-2179. 10.1093/mnras/stae565 . hal-04800652

**HAL Id: hal-04800652**

**<https://hal.science/hal-04800652v1>**

Submitted on 24 Nov 2024






**HAL** is a multi-disciplinary open access archive for the deposit and dissemination of scientific research documents, whether they are published or not. The documents may come from teaching and research institutions in France or abroad, or from public or private research centers.

L'archive ouverte pluridisciplinaire **HAL**, est destinée au dépôt et à la diffusion de documents scientifiques de niveau recherche, publiés ou non, émanant des établissements d'enseignement et de recherche français ou étrangers, des laboratoires publics ou privés.



Distributed under a Creative Commons Attribution 4.0 International License

# Properties of the brightest young stellar clumps in extremely lensed galaxies at redshifts 4 to 5

Matteo Messa <sup>1,2,3</sup>★, Miroslava Dessauges-Zavadsky <sup>2</sup>, Angela Adamo <sup>1</sup>, Johan Richard <sup>4</sup>  
and Adélaïde Claeysens <sup>1</sup>

<sup>1</sup>The Oskar Klein Centre, Department of Astronomy, Stockholm University, AlbaNova, SE-10691 Stockholm, Sweden

<sup>2</sup>Observatoire de Genève, Université de Genève, CH-1290, Versoix, Switzerland

<sup>3</sup>Osservatorio di Astrofisica e Scienza dello Spazio di Bologna, INAF, I-40129, Bologna, Italy.

<sup>4</sup>Univ Lyon, Univ Lyon1, ENS de Lyon, CNRS, Centre de Recherche Astrophysique de Lyon UMR5574, F-69230, Saint-Genis-Laval, France

Accepted 2024 February 19. Received 2024 January 19; in original form 2023 May 15

## ABSTRACT

We study the populations of stellar clumps in three high-redshift galaxies, at  $z = 4.92$ ,  $4.88$ , and  $4.03$ , gravitationally lensed by the foreground galaxy clusters MS1358, RCS0224, and MACS0940, respectively. The lensed galaxies consist of multiple counter-images with large magnifications, mostly above  $\mu > 5$  and in some cases reaching  $\mu > 20$ . We use rest-frame UV observations from the *HST* to extract and analyse their clump populations, counting 10, 3, and 11 unique sources, respectively. Most of the clumps have derived effective radii in the range  $R_{\text{eff}} = 10\text{--}100$  pc, with the smallest one down to 6 pc, i.e. consistent with the sizes of individual stellar clusters. Their UV magnitudes correspond to  $\text{SFR}_{\text{UV}}$  mostly in the range  $0.1\text{--}1 M_{\odot} \text{yr}^{-1}$ ; the most extreme ones, reaching  $\text{SFR}_{\text{UV}} = 5 M_{\odot} \text{yr}^{-1}$  are among the UV-brightest compact ( $R_{\text{eff}} < 100$  pc) star-forming regions observed at any redshift. Clump masses span a broad range from  $10^6$  to  $10^9 M_{\odot}$ ; stellar mass surface densities are comparable and in many cases larger than the ones of local stellar clusters, while being typically 10 times larger in size. By compiling published properties of clump populations at similar spatial resolution between redshifts 0 and 5, we find a tentative evolution of  $\Sigma_{\text{SFR}}$  and  $\Sigma_{M_{\star}}$  with redshift, especially when very compact clumps ( $R_{\text{eff}} \leq 20$  pc) are considered. We suggest that these trends with redshift reflect the changes in the host galaxy environments where clumps form. Comparisons with the local universe clumps/star clusters shows that, although rare, conditions for elevated clump  $\Sigma_{\text{SFR}}$  and  $\Sigma_{M_{\star}}$  can be found.

**Key words:** gravitational lensing; strong – galaxies; high-redshift – galaxies; star clusters; general – galaxies; star formation.

## 1 INTRODUCTION

Since the first deep observations with the *Hubble space telescope* (*HST*), galaxy morphology was recognized to change from disc-like or elliptical into more irregular appearance at increasing redshifts (e.g. Abraham et al. 1996; Brinchmann et al. 1998). In addition, galaxies around the cosmic noon ( $z \sim 1\text{--}3$ ) are characterized by the presence of bright stellar clumps dominating their rest-frame ultraviolet (UV) morphology (e.g. Cowie, Hu & Songaila 1995; van den Bergh et al. 1996). The *JWST* is bringing new insight into the properties of high- $z$  galaxies, especially at the epoch of re-ionization ( $z \gtrsim 7$ ); the first results seem to confirm the overall morphological evolution traced by *HST* at lower redshifts, with galaxies at redshift 7–12 characterized by irregular (yet compact) structures and in a minor part ( $\sim 20$  per cent) by interaction/mergers (Treu et al. 2023).

One of the current main efforts in the community is to understand the link between clump formation (and evolution) and galaxy growth. Initially observed as large structures, with sizes  $\sim 1$  kpc and masses  $\sim 10^8\text{--}10^9 M_{\odot}$  (e.g. Elmegreen et al. 2007; Förster Schreiber et al. 2011a,b; Guo et al. 2012; Soto et al. 2017), stellar clumps are

being recently studied in gravitationally-lensed fields, where lensing allows to reach resolutions down to  $\sim 10$  pc in size and  $\sim 10^6 M_{\odot}$  in mass (e.g. Livermore et al. 2012a; Adamo et al. 2013; Livermore et al. 2015; Johnson et al. 2017; Vanzella et al. 2017a,b; Cava et al. 2018; Vanzella et al. 2019, 2021; Messa et al. 2022; Meštrić et al. 2022; Vanzella et al. 2022b), and thus to investigate clump substructures avoiding overestimates driven by poor resolutions (e.g. Dessauges-Zavadsky et al. 2017; Meng & Gnedin 2020). The exquisite performance of *JWST* is also contributing to increase the resolution and depth at which clump samples are studied (e.g. Vanzella et al. 2022a, c; Claeysens et al. 2023), and recently proved the possibility of observing the progenitors of local globular clusters (Mowla et al. 2022; Claeysens et al. 2023).

Most of clumps at redshift  $z < 3$  may have formed *in situ* within their host galaxies. This scenario is supported by several observational evidence, such as: (1) the redshift evolution of clumpy galaxies, closely following evolution of the overall star formation rate (SFR) volume density and inconsistent with the evolutionary trends of minor and major mergers (Lotz et al. 2011; Shibuya et al. 2016); (2) the presence of numerous clumpy galaxies (at least up to  $z \sim 3$ ) still dominated by disc-like appearance (Shibuya et al. 2016), with comparable disc scale-heights in case of either presence or absence of clumps (Elmegreen & Elmegreen 2006; Elmegreen

\* E-mail: [matteo.messa@inaf.it](mailto:matteo.messa@inaf.it)

et al. 2017); (3) the kinematics of the majority of clumpy star-forming galaxies at cosmic noon being dominated by ordered disc rotation (yet with elevated velocity dispersions, Förster Schreiber et al. 2009; Wisnioski et al. 2015; Rodrigues et al. 2016; Simons et al. 2017; Swinbank et al. 2017; Turner et al. 2017; Girard et al. 2018). Simulations show that such turbulent high- $z$  discs fragment because of gravitational instability and can form gas clouds that turn into stellar clumps (Bournaud et al. 2014; Tamburello et al. 2015; Mandelker et al. 2017); (4) the observations of very young clumps (age  $\lesssim 10$  Myr), inconsistent with an ‘external’ origin (e.g. Förster Schreiber et al. 2011b; Zanella et al. 2015); (5) finally, the stellar mass function of these clumps follows a power law with slope  $-2$  (Dessauges-Zavadsky & Adamo 2018), characteristic of nearby star clusters and H II regions (see e.g. the reviews by Krumholz, McKee & Bland-Hawthorn 2019; Adamo et al. 2020a) and expected for stellar structures formed in a hierarchical manner via turbulence-driven fragmentation (e.g. Elmegreen 2010; Guszejnov, Hopkins & Grudić 2018; Ma et al. 2020). In this scenario, UV-bright clumps are simply star cluster complexes formed in high- $z$  galaxies, and thus likely trace the star-formation process in their host galaxy.

With respect to local stellar clusters and cluster complexes, high-redshift clumps are more extreme systems, usually with elevated star formation rate (SFR) and SFR densities (e.g. Livermore et al. 2015; Messa et al. 2022; Claeysens et al. 2023), and sometimes observed as mini-starburst entities within their host galaxies (Zanella et al. 2015; Iani et al. 2022). Within the *in situ* formation scenario, this difference can be explained by high- $z$  discs fragmenting at much larger scales (and possibly densities) than in local MS galaxies because of their gas-rich and turbulent nature, as suggested by models (e.g. Immeli et al. 2004), numerical simulations of turbulent high-redshift galaxies (e.g. Tamburello et al. 2015; Renaud, Romeo & Agertz 2021; van Donkelaar, Agertz & Renaud 2022), observations of dense giant molecular cloud complexes from CO data in galaxies at  $z = 1$  (Dessauges-Zavadsky et al. 2019, 2023), as well as by observations in nearby analogues (e.g. Fisher et al. 2017a,b; Messa et al. 2019).

While the *in situ* origin seems to explain the formation of  $\sim 70$  per cent of the clumps at redshifts  $z < 3$  (Zanella et al. 2019), it is still possible that galaxies at earlier times were characterized by clumps formed *ex situ*, i.e. by a merger process during which the satellite is stripped and its nucleus appears as a massive clump (e.g. Somerville et al. 2000; Hopkins et al. 2008; Puech 2010; Straughn et al. 2015; Ribeiro et al. 2017). This scenario could be justified by the increasing galaxy (minor and major) merger rate towards higher redshifts (e.g. Lotz et al. 2011), as well as by the increasingly lower number of massive galaxies (Marchesini et al. 2009); simulations show that large-enough galaxy masses are needed for disc fragmentation to happen (e.g. Tamburello et al. 2015). Unfortunately systems before cosmic noon ( $z \gtrsim 4$ ), where violent disc instability is thought to have less impact on clump formation, are currently under-represented in clump studies (e.g. Meštrić et al. 2022). The *JWST* will soon bring a new insight on clump formation at these redshifts, by providing deep, high-resolution rest-frame optical observations (as seen from the first results by e.g. Claeysens et al. 2022; Mowla et al. 2022; Vanzella et al. 2022a).

In this paper, we analyse the clump populations of three bright and highly magnified gravitationally-lensed galaxies at  $z > 3.5$  in order to pave the way for upcoming *JWST* studies of larger samples. The selection, main properties, and observational data of the sample are presented in Section 2; the clump analysis methodology is described in Section 3; results are presented in Section 4 and discussed,

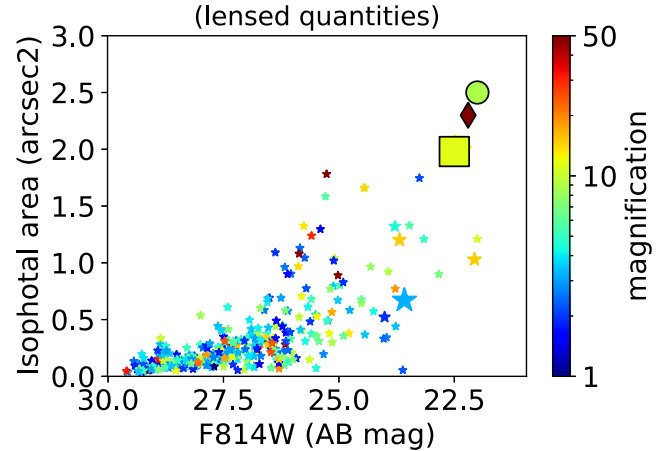


**Figure 1.** Observed (lensed) rest-frame UV magnitudes and angular area covered by spectroscopically confirmed  $z > 3.5$  galaxies gravitationally lensed by galaxy clusters taken from the literature (see text for details). The sizes of the markers is proportional to the number of clumps observed in the galaxy. The final selection of three galaxies analysed in the current work are highlighted by the following markers: a circle (MS1358), a diamond (RCS0224), and a square (MACS0940).

also in the context of other literature works, in Section 5; finally, the main details of this analysis are summarized in Section 6. Throughout this paper, we adopt a flat  $\Lambda$ -CDM cosmology with  $H_0 = 68 \text{ km s}^{-1} \text{ Mpc}^{-1}$  and  $\Omega_M = 0.31$  (Planck Collaboration et al. 2014), and the Kroupa (2001) initial mass function. All quoted magnitudes are on the AB system.

## 2 SAMPLE AND DATA

### 2.1 Galaxy sample

We search for spatially extended lensed galaxies at  $z > 3.5$ , with spectroscopically-confirmed redshifts. These criteria are chosen to characterize subgalactic scales at redshifts where, as outlined in the introduction, we may expect different formation mechanisms than cosmic noon. The search is restricted to cluster lensing to allow for larger magnifications across the full extent of the arcs. The sample of clusters is taken from the full MASSive Clusters Survey (MACS; e.g. Ebeling et al. (2010); Repp, Ebeling & Richard (2016)), as well as other clusters taken from the LoCuSS (Richard et al. 2010), CLASH (Postman et al. 2012), Frontier Fields (Lotz et al. 2017), and RELICS (Coe et al. 2019) cluster samples. In Fig. 1, we observe how, while the typical population of background lensed galaxies behind many massive galaxy clusters is distributed around apparent (and magnified) rest-frame UV magnitudes in the range 26–30 mag (see also Richard et al. 2021, Claeysens et al. 2022), three galaxies clearly stand out in terms of brightness and angular area. Those galaxies are located beyond the lensing clusters MS 1358+62 (at  $z_{\text{cl}} = 0.33$ ), RCS 0224–0002 (at  $z_{\text{cl}} = 0.77$ ), and MACS J0940.9+0744 (at  $z_{\text{cl}} = 0.34$ ); the lensed systems are in the redshift range  $z = 4$ –5 and are all magnified by large factors ( $\mu > 5$ ). The selected targets are typical of their redshift, in terms of masses and SFRs (see Sections 2.1.1, 2.1.2, and 2.1.3) but appear ‘clumpy’, i.e. host more than one bright clump (in Fig. 1, the marker size is proportional to the number of observed clumps), due to their large magnification factors, making them optimal candidates for the study of star formation at small subgalactic scales, down to 10 pc (see Section 4.1). In addition, their

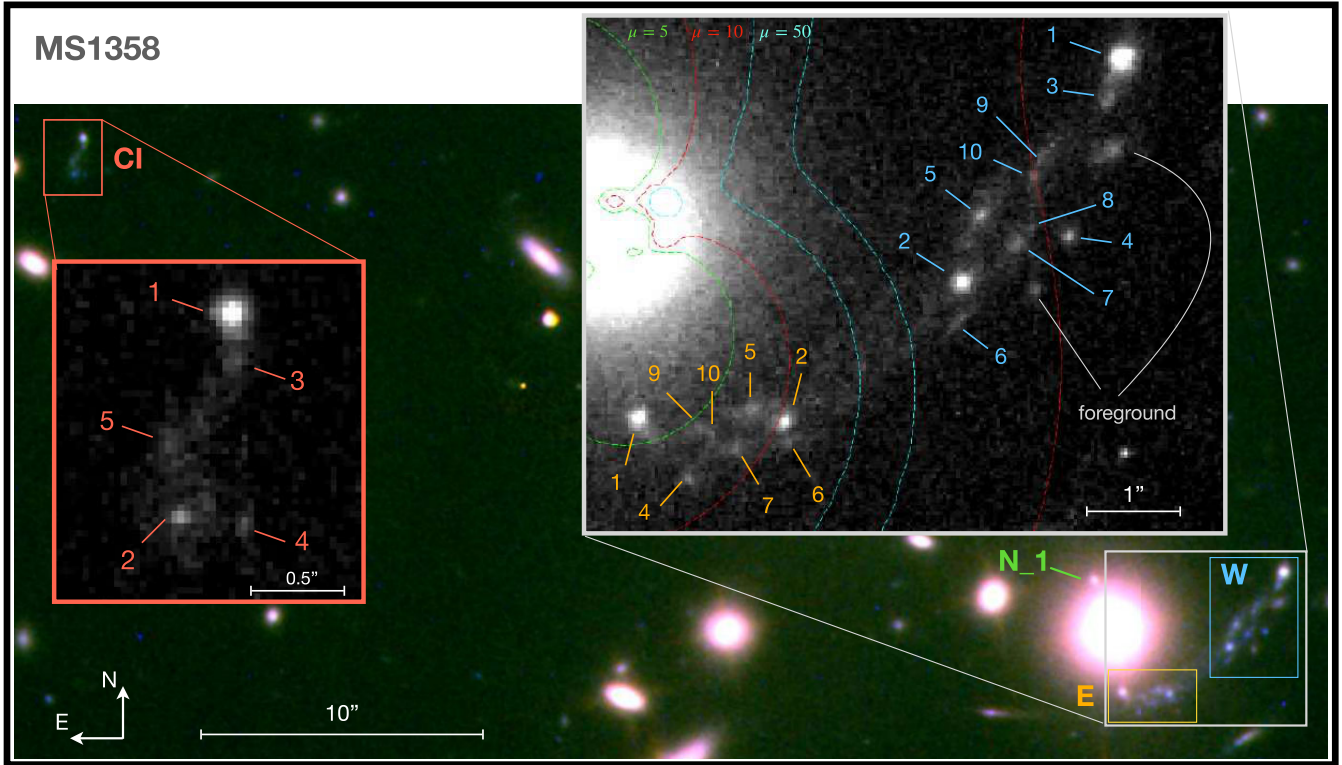


**Figure 2.** RGB composite (r: *F160W*, g: *F110W*, b: *F775W*) of the galaxy cluster field MS 1358+62, containing the  $z = 4.93$  lensed western (W) and eastern (E) arcs and their counter-image (CI). The zoomed-in inset, showing the observations in the reference *F775W* filter, highlights the positions and names of the extracted stellar clumps in all the different multiple images. A partial northern image (N) of the lensed galaxy contains only one clump and is labelled as ‘N\_1’. Dashed lines show regions of constant magnifications at  $\mu = 5, 10,$  and  $50$  (green, red, and cyan, respectively) at the redshift of the lensed arcs. Reference angular scale are given; the image is aligned with north-up and east-left.

large magnified observed brightness makes them ideal targets for future *JWST* observations.<sup>1</sup>

We summarize below the main properties of these galaxies from previous studies in the literature; for simplicity, we will use the shortened names of the galaxy clusters as the names of the high- $z$  lensed galaxies we analyse in this work.

### 2.1.1 MS1358

The  $z = 4.92$  lensed galaxy behind MS 1358+62 galaxy cluster was first discovered and studied by Franx et al. (1997). The galaxy rest-frame UV/optical morphology is dominated by several compact star-forming regions. Fitting the broad-band SED from *HST* and *Spitzer* imaging, Swinbank et al. (2009) derived a total mass  $M_\star = (4.7 \pm 1.3) \times 10^8 M_\odot$ <sup>2</sup> from a young stellar population ( $14 \pm 7$  Myr) with subsolar metallicity ( $Z = 0.2 Z_\odot$ ); the stellar extinction is consistent with being close to zero,  $E(B - V) = 0.05 \pm 0.05$  mag. A star formation rate of  $\text{SFR} = 28 \pm 5 M_\odot \text{yr}^{-1}$  was derived from the [O II] emission-line flux (Swinbank et al. 2009). The galaxy is characterized by the presence of two main subgalactic star-forming

regions (IDs: 1 and 2 in Fig. 2) accounting for  $12 \pm 1 M_\odot \text{yr}^{-1}$  in SFR. IRAM PdBI observations in CO(5–4) emission suggest that the galaxy has a large gas fraction,  $f_{\text{gas}} = 0.6$  (Livermore et al. 2012b), similarly to what is observed in  $z \geq 3$  galaxies (Dessauges-Zavadsky et al. 2020).

### 2.1.2 RCS0224

A lensing-magnified arc at  $z = 4.88$  in the RCS 0224-0002 cluster, it was first discovered as a bright Ly $\alpha$  halo by Gladders, Yee & Ellingson (2002). Swinbank et al. (2007) studied the rest-frame ultraviolet and optical properties of the galaxy by combining *HST* imaging to VIMOS and SINFONI spectroscopy, deriving a dynamical mass of  $\sim 10^{10} M_\odot$  (within the estimated 2 kpc intrinsic size of the galaxy) and a star formation rate of  $8.2 \pm 1.4 M_\odot \text{yr}^{-1}$  (using [O II] observations<sup>3</sup> covering only the central and western, C and W, images in Fig. 3). A further study with MUSE suggested that the detected emission lines are powered by a young ( $< 5$  Myr) and low-metallicity ( $Z \lesssim 0.05 Z_\odot$ ) stellar population (Smit et al. 2017).

### 2.1.3 MACS0940

MACS0940 at  $z = 4.03$ , first studied by Leethochawalit et al. (2016) is observed as a strongly stretched arc made of two mirrored images (see Fig. 4). Two complete counter-images of the same galaxy are

<sup>1</sup>*JWST* observations with NIRSpec-IFU and NIRCам imaging have been approved for these targets, GO program 3433.

<sup>2</sup>The original values of mass ( $M_\star = 7 \times 10^8 M_\odot$ ) and star formation rate ( $\text{SFR} = 42 M_\odot \text{yr}^{-1}$  for the entire galaxy and  $\text{SFR} = 18 M_\odot \text{yr}^{-1}$  for the two brightest clumps) were derived by Swinbank et al. (2009) assuming a Salpeter (1955) IMF and are here converted to match the assumption of Kroupa (2001) IMF used throughout the current paper.

<sup>3</sup>This value has been adapted from the original  $12 \pm 2 M_\odot \text{yr}^{-1}$  to translate from Kennicutt (1998) to the Kennicutt & Evans (2012) calibrations.



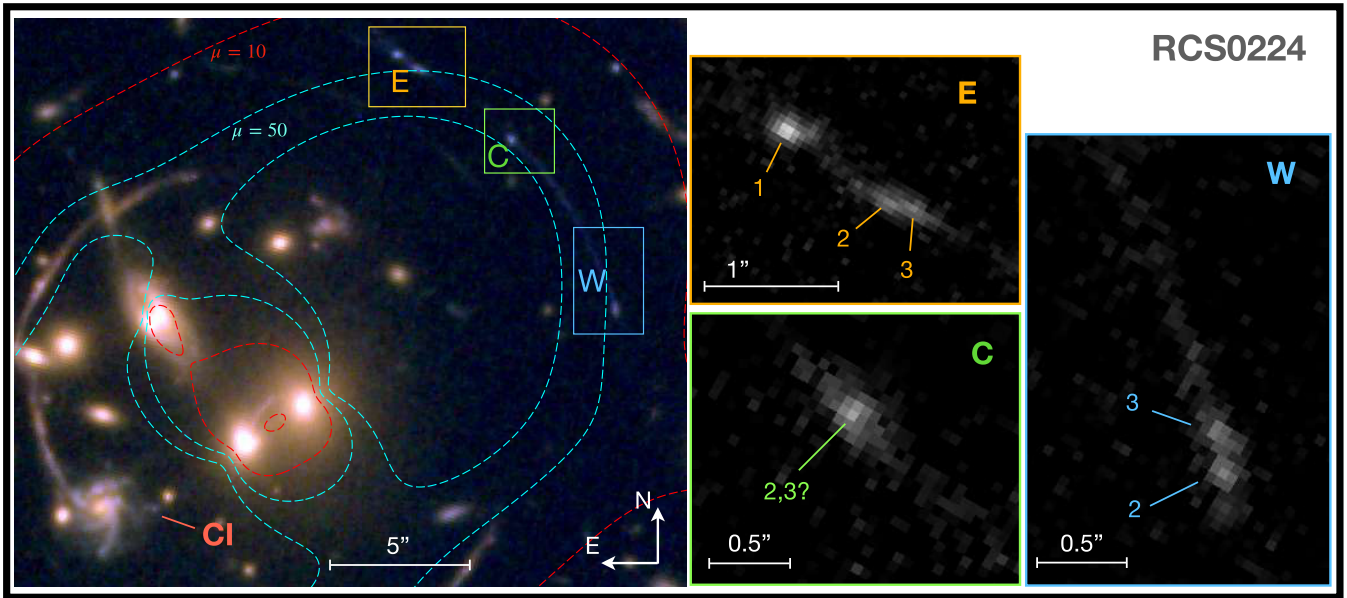


**Figure 3.** Same as Fig. 2, for RCS0224 (r:  $F160W$ , g:  $F125W$ , b:  $F814W$ , zoom-ins:  $F814W$ ). According to the lens model, the clump seen in the central (C) image is consistent with the position of either clump 2 or 3; the study of clump properties suggests that what is observed is a counter-image of clump 2 (see Section 5.1 and Table 3).

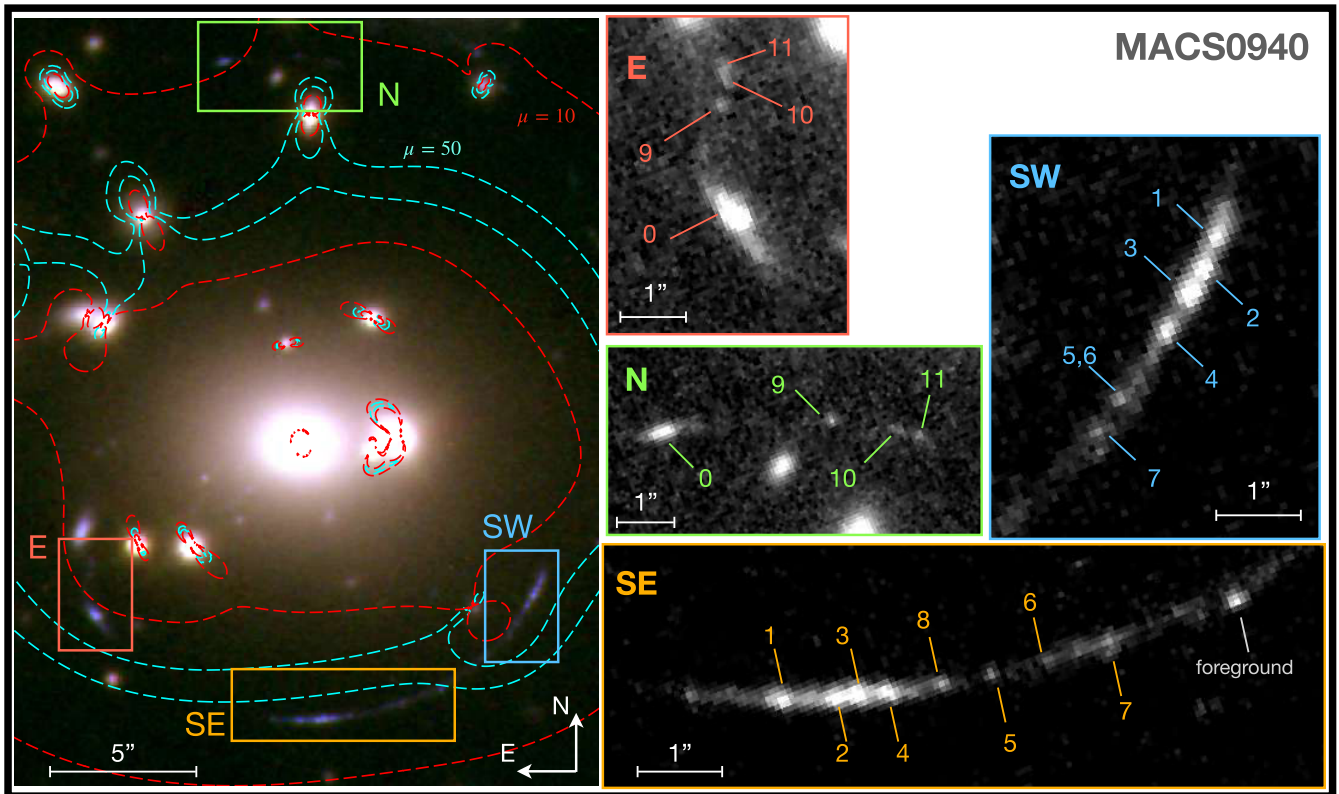


**Figure 4.** Same as Fig. 2 for MACS0940 (r:  $F160W$ , g:  $F125W$ , b:  $F814W$ , zoom-ins:  $F814W$ ). According to the lens model of the system, the SE and SW arcs (and all the clumps they host) are different lensed images of the main galaxy (labelled as ‘0’ in the N and E fields). The clumps 9, 10, and 11, observed in the N and E fields, do not have counterparts in the SE and SW fields.

seen northern and eastern from the arc. The galaxy is characterized by a bright  $\text{Ly}\alpha$  halo (Claeysens et al. 2019), suggesting recent episodes of star formation. Bright compact sources are clearly visible along the arc in rest-frame UV observations.

## 2.2 Hubble Space Telescope (HST) observations

*HST* observations with WFC2, ACS/WFC, and WFC3/IR are available on the *HST* MAST archive (see Data Availability section at

**Table 1.** Galaxy sample and *HST* data: (1) ID of the galaxy (we remind that we are using the name of the hosting galaxy clusters as names/IDs of the lensed arcs studied); (2) redshift of the galaxies from Franx et al. (1997), Gladders, Yee & Ellingson (2002), and Leethochawalit et al. (2016); (3) number of lensed images analysed (in parenthesis the number of counter-images not included in the clump study); (4) range of magnification values covered by the galaxy; (5) references for the lens models; (6) reference filter used to extract the size and UV magnitude of the clumps; (7) other filters used to derive the broad-band SED of the clumps. <sup>†</sup>All filters are from either WFC3 or ACS, except *F606W* from WFPC2. <sup>‡</sup>*F775W* is used instead of *F814W* as the reference filter for MS1358 because of its longer exposure time, providing better signal-to-noise.

Galaxy (1)	$z$ (2)	$N_{\text{img}}$ (3)	$\mu_{\text{range}}$ (4)	Lens model ref. (5)	$F_{\text{ref}}^{\dagger}$ (6)	Other filters <sup>†</sup> (7)
MS1358	4.92	3 (1)	3–20	Swinbank et al. (2009)	<i>F 775 W</i> <sup>‡</sup>	<i>F625W, F814W, F850LP, F110W, F160W</i>
RCS0224	4.88	3 (1)	30–85	Swinbank et al. (2007), this work	<i>F 814 W</i>	<i>F606W, F125W, F160W</i>
MACS0940	4.03	4 (0)	6–33	Clayssens et al. (2019); Richard et al. (2021)	<i>F 814 W</i>	<i>F606W, F125W, F160W</i>

**Table 2.** Main properties of the observations in the reference filter for each galaxy: (1) galaxy ID; (2) reference filter; (3) rest-frame pivotal wavelength; (4) exposure time; (5) & (6) extraction and completeness limits for a point-like source within the galaxy, as described in Section 3.2.1; note that these values are corrected for the Galactic reddening.

Galaxy (1)	$F_{\text{ref}}$ (2)	$\lambda_{\text{rest}}$ [Å] (3)	$t_{\text{exp}}$ [s] (4)	PSF [arcsec] (5)	$\text{lim}_{\text{ext}}$ [mag] (6)	$\text{lim}_{\text{com}}$ [mag] (7)
MS1358	<i>F775W</i>	1300	5470	0.10	27.7	27.9
RCS0224	<i>F814W</i>	1370	2168	0.11	26.5	27.1
MACS0940	<i>F814W</i>	1600	7526	0.12	27.3	27.4

the end of the publication for details about program IDs). The list of filters used is given in Table 1. For each galaxy, we choose a reference filter, covering the rest-frame UV wavelengths (see Table 2), where we measure the size and UV luminosity of the clumps (as described in Section 3.2); the other filters are used to infer the broad-band SED of the clumps (see Section 3.4). Individual flat-fielded and CTE-corrected exposures were aligned and combined in single images using the *AstroDrizzle* procedure from the *DrizzlePac* package (Hoffmann et al. 2021). The astrometry was aligned to the *Gaia* DR2 (Gaia Collaboration et al. 2018).

We model the instrumental point-spread function (PSF) from isolated bright stars within the field of view of the observations. In each filter, we fit the selected stars with an analytical function described by a combination of Moffat, Gaussian, and 4<sup>th</sup> degree power-law profiles. Such a generic combination is chosen to mitigate possible bias introduced by the choice of a specific function. The fits provide good descriptions of the stars up to a radius of  $\sim 0.8$  arcsec, i.e. more than  $10\times$  larger than the half-width at half-maximum (HWHM) of PSF in the reference filters (the full width at half-maximum, FWHM, of the reference filters are 0.10, 0.11, and 0.12 arcsec for MS1358, RCS0224, and MACS0940, respectively, see Table 2). The modelled PSF is used to derive the size and luminosity of the clumps, as described in detail in Section 3.2.

### 2.3 Gravitational lens models

Our study relies on the reconstruction of intrinsic properties of the identified clumps, accounting for the anisotropic lensing magnification which is estimated from a lens model.

As a starting point, we make use of existing mass models of the cluster cores (references in Table 1), which include the lensed arcs as constraints. In summary, these models use a parametric mass distribution describing the cluster-scale and galaxy-scale mass components of the clusters as a combination of double pseudo isothermal elliptical (dPIE) profiles. The models are optimized with

the *Lenstool* Jullo et al. (2007) software<sup>4</sup> based on multiple imaged constraints, similarly to the modelling performed in e.g. Richard et al. (2014). In the case of the older models for MS1358 and RCS0224, we have performed a new optimization using the latest version (v8) of *Lenstool*.

In all cases, individual clumps identified as mirrored images in the three lensed arcs are individually used as constraints in the model, ensuring a very good reproduction of the images. The rms between the observed and predicted locations of the images used in the model is 0.06, 0.08, and 0.24 arcsec for MS1358, RCS0224, and MACS0940, respectively.

The outcome of the *Lenstool* optimization is a statistical sample of mass models sampling the posterior distribution function of the model parameters. We make use of both the best model (achieving the lowest rms) and the range of mass models to estimate the magnification factors (along each direction) at each position across the arc and their 68 per cent percentile error. The range of magnification factors obtained is summarized in Table 1.

## 3 DATA ANALYSIS

### 3.1 Clump extraction

Clump candidates have been extracted by running *SExtractor* (Bertin & Arnouts 1996), requiring  $3\sigma$  detections in at least 4 pixels (px) in background subtracted images (where the background is evaluated on a 30 px scale) in the reference filter. In order to check for ‘redder’ sources that could be missed in the reference filter, we ran *SExtractor* with the same set of parameters also in all the other available filters in each galaxy; this test did not produce any further sources. The colours of the clumps and the lens models have been used to identify interlopers, mainly bright compact sources at different redshifts, among the extracted sources (some examples are highlighted in Figs 2 and 4).

The extracted clumps are shown together with their assigned IDs in Figs 2, 3, and 4. The lens models predictions were used to match the same clump over different images. Ten and eight clumps are observed in the western (W) and eastern (E) arcs of MS1358, respectively; only five of them are clearly visible in the counter-image (CI). The brightest clump (ID:1) is the only one visible in the northern image (N.1). RCS0224 appears in the eastern image (E) as composed of two bright regions, one of which is composed by two subclumps. Only one of such regions (containing clumps 2 and 3) is visible in the western image (W); the central image (C) is instead characterized by a single source (either clump 2 or 3), with a very

<sup>4</sup>Publicly available at <https://projets.lam.fr/projects/lenstool/wiki>

high magnification. The counter-image (CI) of RCS0224 appears as a single source, where clumps are indistinguishable. MACS0940 counts a total of eight clumps in the eastern arc (SE), the one with the largest magnification overall. Only six of those clumps are seen in the western arc<sup>5</sup> (SW), while both the eastern and northern counter-images (E and N) look like a single bright source (consistent with the superposition of the brightest clumps, IDs: 1, 2, 3, and 4) surrounded by diffuse light and by three sources (IDs: 9, 10, and 11, not seen in the arcs).

### 3.2 Clump modelling

Clumps are modelled on the image plane, fitting their sizes and fluxes on the observed data of the reference filter; such quantities are later converted into intrinsic values, using the magnification maps produced by the lens model (Section 2.3). The clump modelling follows accurately the methodology applied to the study of stellar clumps in the  $z = 1$  galaxy A521-sys1 (Section 3.2 of Messa et al. 2022), of which we summarize here the main features. We assume that clumps have Gaussian profiles in the image plane, and therefore we fit a model consisting of 2D Gaussian functions, convolved to the instrumental point spread function (i.e. the response of the instrument), to obtain their observed profiles.

We performed clump fitting in  $9 \times 9$  px cut-outs centred on each of the clumps, where a 1st degree polynomial function is added to account for the galaxy background luminosity: both size (including axis-ratio and orientation for elliptical sources) and flux of the clumps are left as free parameters of the fit in the reference filter. The best-fit models and residuals are shown in Appendix A. The clump shape is then kept fixed in the other filters, where only the source flux is fitted, under the assumption that the intrinsic clump shape is the same in all bands. In order to reduce the possibility of contamination from nearby bright sources, the brightest clumps were fitted first, and then their best-fitting model subtracted from the data. The fitted fluxes, in units of  $e^-/s$ , are converted into observed AB magnitudes by considering the instrumental zero-points and by subtracting the reddening introduced by the Milky Way in each of the filters. The (observed) effective radius of the clumps,  $R_{\text{eff,obs}}$ , here defined as the radius enclosing half of the source's luminosity, is equal to the (circularized) full width at half-maximum, in the current assumption of Gaussian profiles. In the occurrence of multiple clumps separated by less than 5 px, a single fit is performed in cut-outs large enough to include all sources (typically  $15 \times 15$  px).

As already discussed in Messa et al. (2019, 2022), the oversampling of the *HST* PSF (FWHM  $\sim 2$  px in the filters considered in this work) allow to resolve subpixel clump sizes. By inserting mock clumps of various sizes in the image frames and fitting them as for the real clumps, we derive the minimum resolvable size,  $\sigma_{\text{min}} = 0.40$  px for MS1358 and MACS0940, and  $\sigma_{\text{min}} = 0.45$  px for RCS0224. These limits, converted into physical sizes at the redshift of the galaxies, are highlighted in the top panels of Fig. 5. We refer to Appendix C of Messa et al. 2022 for more details on the process of estimating the minimum resolvable size.

#### 3.2.1 Completeness of the sample

We separately tested the completeness we reached in extracting and analysing our samples. In order to test the sensitivity of our extraction

process, we insert, one by one, 1500 synthetic clumps at random positions within the region covered by the lensed systems (in the reference filter used in the original extraction, Section 3.1). The clumps are modelled as symmetric Gaussians and divided into three 'size groups', with  $\sigma = 0.4$  (0.45 for RCS0224), 1.0, and 2.0 px; the first value corresponds to the minimum resolvable size (see Section 3.2), while the last encompasses the largest clumps observed in the samples (see Fig. 5, top row). Clumps are randomly drawn from a flat distribution in magnitudes. For each realization, we run SExtractor with the same sets of parameters used in Section 3.1, and we check if the synthetic clump has been extracted. For each of the three sizes chosen, we consider as extraction limit,  $\text{lim}_{\text{ext}}$  the magnitude below which the fraction of extracted clumps goes above 90 per cent.

In order to test the reliability of the derived photometry, we estimate the completeness of the sample in a second way, following the method described in Appendix D of Messa et al. (2022); the same synthetic clumps used to estimate the extraction limits are photometrically analysed in the same way as the real sources. We consider as good sources the ones where the relative error on the recovered flux is below 50 per cent,  $\text{flux}_{\text{rel}} = |\text{flux}_{\text{in}} - \text{flux}_{\text{out}}|/\text{flux}_{\text{in}} < 0.5$ . We consider as completeness limits,  $\text{lim}_{\text{com}}$ , the magnitudes below which the fraction of good sources recovered goes above 80 per cent. All the extraction and completeness limits are compared to the photometry of the clumps in the sample in Fig. 5 (top row). The limits in the case of point-like clumps are also reported in Table 2.

### 3.3 Conversion to intrinsic sizes and magnitudes

In order to recover the intrinsic clumps' properties, we considered the magnification map produced by the best-fit lens model of each galaxy; we used as reference amplification,  $\mu_{\text{tot}}$ , the median amplification value found in the region centred on each clump coordinates and extending within one FWHM of its size. We use the standard deviation of amplification values found in the same region as an estimate of the magnification uncertainty associated to the clump position. To estimate the uncertainty associated to the magnification map, we consider, for each cluster, the  $1\sigma$  interval (16<sup>th</sup> to 84<sup>th</sup> percentiles) of the amplification values found in the 500 lens model variations described in Section 2.3. The two magnification uncertainties are combined (by the sum of the squares) into a final uncertainty. We note that the uncertainty from the 500 'variation' maps is the one usually dominating the final value.

The observed magnitudes are converted into absolute ones by subtracting the distance modulus and adding the  $k$  correction, a factor  $2.5 \log(1+z)$ ; the amplification is accounted for by adding  $2.5 \log(\mu_{\text{tot}})$ , converting the magnitude into the intrinsic value.

We consider three cases when measuring the intrinsic effective radius,  $R_{\text{eff}}$ , following the methodology already used and discussed in the literature (e.g. Vanzella et al. 2017a; Claeysens et al. 2023). If the clump is resolved along both minor and major axis in the image plan, we simply divide the observed  $R_{\text{eff,obs}}$  by the square-root of the clump amplification. If the clump is un-resolved along the transversal direction of the magnification, we consider as informative only the size measured in the shear direction, and we divide the latter by the tangential component of the magnification ( $\mu_{\text{tan}}$ ). Finally, if the clump is unresolved in both directions, we divide the observed  $R_{\text{eff,obs}}$  (consistent with the instrumental PSF) by  $\mu_{\text{tan}}$  to derive a size upper limit. In the last two cases, the underlying assumption is that the clump has approximately a circular shape in the source plane. The final uncertainties on the intrinsic properties combine both photometric and magnification uncertainties via the root sum squared.

<sup>5</sup>Due to the uncertainties in the clumps predicted positions given by the lens model, one source is consistent with being the counterpart of either SE\_5 or SE\_6 and was labelled SW\_5,6 to reflect this.



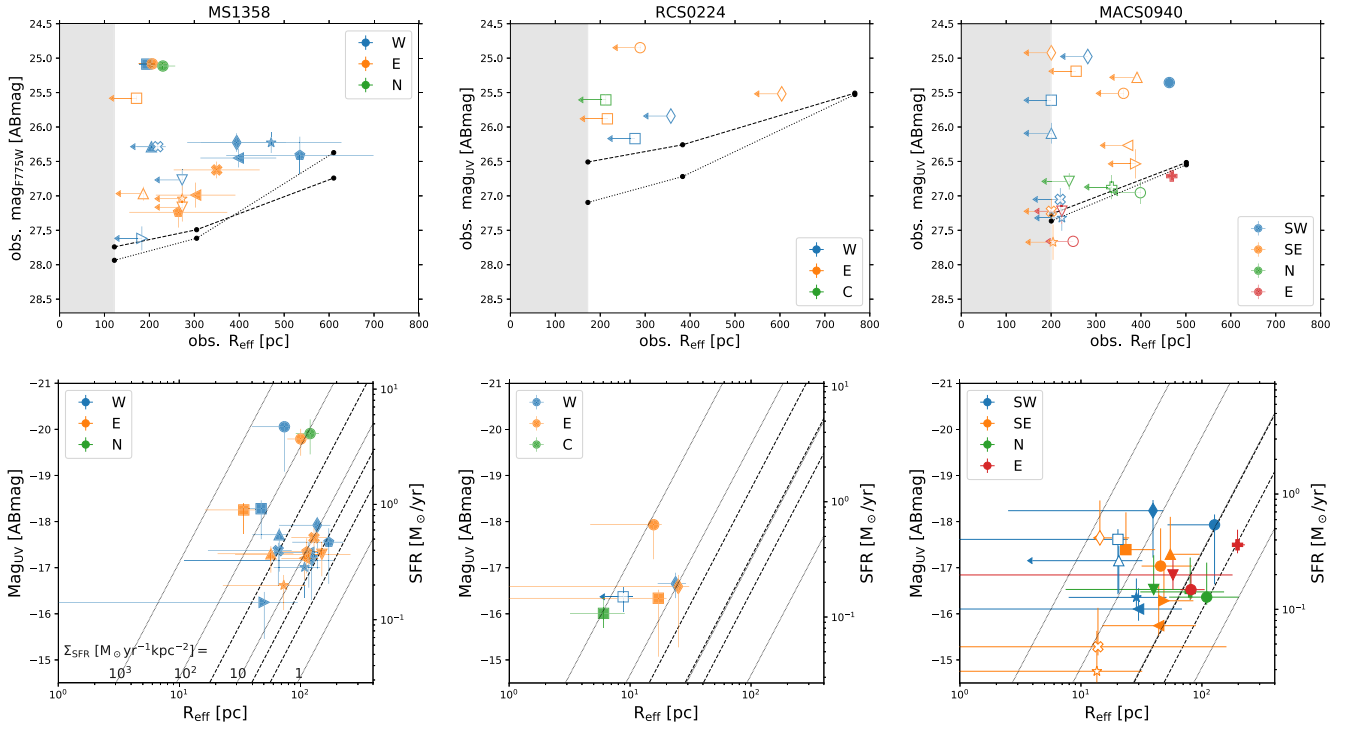


**Figure 5.** (*Top panels*): observed sizes and magnitudes (in the reference filter) for all the clumps in this study. Estimates of the observed sizes consider the angular diameter distance of the host galaxy but do not take into account their lensing magnification. The grey shaded areas highlight the size of the regions below our resolution limits. Black dot markers (connected by dashed lines) indicate the extraction limits for each of the simulated sizes considered (see main text in Section 3.2.1 for details); similarly, markers connected by dotted lines are used to indicate completeness limits. (*Bottom panels*): Intrinsic sizes and magnitudes of the clumps. UV magnitudes have been converted into  $\text{SFR}_{\text{UV}}$  values using the Kennicutt & Evans (2012) relation on the right-hand side of each panel. Uncertainty bars combine both photometric and lensing uncertainties. The extraction limits shown in the top panels have been converted here to surface brightness limits (dashed lines, each line corresponds to the limit derived for one simulated size). Solid grey lines are of constant SFR surface density for 1, 10,  $10^2$ , and  $10^3 \text{ M}_{\odot} \text{ yr}^{-1} \text{ kpc}^{-2}$ . In all panels, open symbols are used for upper limits and same markers are used for the same clumps in different counter-images.

### 3.4 Broad-band SED fitting

We use the broad-band photometry to estimate the clumps’ masses. Following the methodology of Messa et al. (2022) and Claeysens et al. (2023), photometry in the filters other than the reference one is performed by assuming that each source has the same observed size (derived in Section 3.2) in all the bands, and thus fitting only the flux and the background. Due to the elevated redshift of the sources, the available *HST* filters cover only the rest-frame wavelength range  $\sim 1000\text{--}3000 \text{ \AA}$ . As a consequence our SED-derived values are UV-weighted quantities. In particular, ages and extinctions are only poorly constrained; on the other hand, mass estimates are more robust and within a factor of a few correct (see also Messa et al. 2022 for the robustness of mass estimates over different model assumptions).

To mitigate the effects of degeneracies between parameters of the fit (in particular ages, extinctions, metallicities, and star formation histories, SFHs), we limit the number of free parameters. First of all, we fixed the metallicity of the stellar models; following Stark et al. (2009), we use a subsolar metallicity,  $Z = 0.2 Z_{\odot}$ . Smit et al. (2017) suggests that the nebular C IV lines observed in RCS0224 must come from a young stellar population with metallicity  $Z = 0.05 Z_{\odot}$  or lower. For this reason, we perform, for all galaxies, a second ‘control’ fit using stellar models with metallicity  $Z = 0.02 Z_{\odot}$ . As a second strong assumption, we consider SFHs described by a 10 Myr continuous star formation. This choice is driven by the sizes of the clumps (Section 4.1), larger than typical stellar clusters (for which an instantaneous burst is usually assumed); assuming longer histories,

like a 100 Myr continuous star formation, would lead to larger masses on average (as already found by, e.g. Adamo et al. 2013; Messa et al. 2022; Claeysens et al. 2023). We use the stellar models from the Yggdrasil stellar population synthesis code<sup>6</sup> (Zackrisson et al. 2011), based on Starburst99 Padova-AGB tracks (Leitherer et al. 1999; Vázquez & Leitherer 2005), with a universal Kroupa (2001) IMF (in the mass interval 0.1–100  $\text{M}_{\odot}$ ), processed through Cloudy (Ferland et al. 2013), assuming a 50 per cent nebular covering fraction, to obtain the evolution of the nebular continuum and line emission produced by the ionized gas. The model spectra, at each age, are attenuated with a colour excess ranging between  $E(B - V) = 0\text{--}1$  mag, using the Calzetti et al. (2000) law, before being convoluted with the filter throughput. We do not use the differential expression formulated by Calzetti et al. (2000), but we apply the same reddening to both stellar and nebular emission, assuming that stars and gas are well mixed. We check *a-posteriori* that the accepted solutions for the SED fit have low extinctions,  $E(B - V) \leq 0.4$  mag in most cases. Age, mass and extinction are left as free-parameters in the SED fitting process. Best-fit parameters are given by the model with the lowest reduced  $\chi^2$  ( $\chi_{\text{red},\text{min}}^2$ ). Their uncertainties are given by the entire range of solutions whose reduced  $\chi^2$  satisfies  $\chi_{\text{red}}^2 \leq 2 \times \chi_{\text{red},\text{min}}^2$ ; this value was chosen by inspecting the fit results, as it encompasses similarly-good solutions. Like it was the case for magnitudes in

<sup>6</sup>Yggdrasil models can be found at <https://www.astro.uu.se/~ez/yggdrasil/yggdrasil.html>



Section 3.3, de-lensed masses are derived by dividing the observed mass of each clump by its total magnification.

## 4 RESULTS

### 4.1 Clumps sizes and luminosities

The observed (i.e. not de-lensed and therefore not ‘intrinsic’) clump sizes and magnitudes are shown in the top row of Fig. 5, where they are compared to the extraction and completeness limits described in Section 3.2.1. The magnitude ranges are similar among the different galaxies ( $\sim 28$ – $25$  AB mag) and, in the great majority of cases, the analysed clumps are above the completeness limit, suggesting that their photometry is robust. The shallower extraction and completeness limits in RCS0224 (consistent with the exposure time of this galaxy being the shortest, see Table 2) cause the average clump magnitude in this galaxy to be bright ( $\sim 26$ – $25$  mag). This result may suggest that we are missing clumps at lower surface brightness. A shaded-grey area in the plot marks the region below the size lower limits discussed in Section 3.2; in the absence of gravitational lensing, we wouldn’t be able to study clumps below  $\sim 100$ – $200$  pc scales.

The intrinsic (i.e. de-lensed) clump sizes and magnitudes are shown in the bottom row of Fig. 5 and are reported in Table 3. Intrinsic sizes are smaller than 200 pc and in many cases reach values close to 10 pc; in particular, due to the magnification factors associated to our galaxies, we are studying clumps at scales comparable to large individual star clusters in RCS0224 ( $R_{\text{eff}} = 5$ – $25$  pc) and slightly larger scales in the other two cases, consistent with the sizes of compact star-forming regions ( $R_{\text{eff}} = 13$ – $200$  pc in MACS0940 and  $R_{\text{eff}} = 30$ – $150$  pc in MS1358). The rest-frame UV magnitudes, on the y-axis of Fig. 5 (bottom panels), have also been converted into a SFR value (using the conversion factors from Kennicutt & Evans 2012), as this is a commonly used parameter in high- $z$  clump studies. In the same panels, we show lines of uniform SFR surface densities ( $\Sigma_{\text{SFR}} = 1, 10, 10^2, 10^3 M_{\odot} \text{ yr}^{-1} \text{ kpc}^{-2}$ ). The extraction limits described above, when translated into surface-brightness limits (dashed lines), correspond to  $\Sigma_{\text{SFR}} \sim 10 M_{\odot} \text{ yr}^{-1} \text{ kpc}^{-2}$ . In all cases, the completeness is above the typical  $\Sigma_{\text{SFR}}$  values of clumps in local main sequence galaxies  $\sim 0.6 M_{\odot} \text{ yr}^{-1} \text{ kpc}^{-2}$  (Kennicutt Robert C. et al. 2003; Livermore et al. 2015).

In some cases, we are not able to robustly constrain the clump properties, mainly due to very large uncertainties on the magnification. Those cases are discussed for each galaxy individually in Section 5.1 and are then removed from following analyses. A detailed discussion of clump intrinsic properties for each of the galaxies is given in Section 5.1, while a comparison of clump sizes and SFRs with other literature samples is given in Section 5.2.

### 4.2 Clumps masses

We report in Table 3 the properties derived from the broad-band SED fitting of the clumps. Due to the large uncertainties on ages and extinctions, we choose to provide only a range of allowed values for those two degenerate properties. The majority of clumps are consistent with being as young as  $\sim 1$  Myr (this is consistent with the observations of bright nebular emission in Ly $\alpha$ , C IV, and [O II] reported in literature, e.g. Smit et al. 2017; Claeysens et al. 2019) but with equally-probable solutions at ages as old as  $\sim 100$  Myr. In the latter case, a star formation longer than what is considered should be accounted for in order to explain the nebular emission.

The derived colour excesses mainly span the range  $E(B - V) = 0.0$ – $0.3$  mag (up to 0.6 mag in MS1358), suggesting low overall extinctions in these galaxies.

Model degeneracies have lower effect on clump masses, which we provide as best-fit values; intrinsic masses are affected by uncertainties on the lens model, as seen for absolute magnitudes in the previous section. Derived clump masses span the range  $M = 10^6$ – $10^9 M_{\odot}$ . Using models with lower metallicity ( $Z = 0.02 Z_{\odot}$ ) than the reference one ( $Z = 0.2 Z_{\odot}$ ) we get, on average, the same masses (within 0.1 dex) as the ones reported in Table 3 for MS1358 and MACS0940. In the case of RCS0224, we get 0.3 dex larger masses associated to older best-fit ages, on average. We also expect that, using models with longer SFHs, we would derive, on average, larger masses (e.g. by  $\sim 0.1$  dex for 100 Myr continuous star formation, see Messa et al. 2022). Both these alternative assumptions would cause mass differences that are within the mass uncertainty ranges reported in Table 3.

The comparison of clump masses to their sizes in Fig. 6 reveals that we are looking at very dense systems; they have, on average, mass surface densities  $\Sigma_{M_{\star}} \sim 10^3 M_{\odot} \text{ pc}^{-2}$ , similar to those of stellar clusters in local galaxies (e.g. Brown & Gnedin 2021) but on scales which are up to  $\sim 10$  times larger, i.e. up to  $\sim 100$  pc in the case of MS1358. The densest systems observed in these three high- $z$  galaxies reach values  $> 10^4 M_{\odot} \text{ pc}^{-2}$ , matching the most extreme stellar ensembles observed at any redshift (see the discussion in Section 5.2).

The combination of mass ( $M_{\star}$ ) and size ( $R_{\text{eff}}$ ) of the clumps provides an estimate of their crossing time, defined as (Gieles & Portegies Zwart 2011):

$$T_{\text{cr}} \equiv 10 \left( \frac{R_{\text{eff}}^3}{GM_{\star}} \right)^{\frac{1}{2}}. \quad (1)$$

In local studies of stellar clusters, crossing times are compared to cluster ages to derive the so-called ‘dynamical age’ of clusters ( $\Pi \equiv \text{Age}/T_{\text{cr}}$ ); a value  $\Pi > 1$  indicates that the stars in the system remained clustered together, without freely expanding into their surroundings, for a time longer than their crossing time, implying that the system is likely gravitationally bound (e.g. Gieles & Portegies Zwart 2011; Ryon et al. 2015, 2017; Krumholz, McKee & Bland-Hawthorn 2019; Brown & Gnedin 2021). The same kind of analysis has been recently applied to the study of high- $z$  stellar clumps (e.g. Vanzella et al. 2021; Messa et al. 2022; Vanzella et al. 2022a; Claeysens et al. 2023). Crossing times for the clumps in the three galaxies of the current sample are reported in Table 3. Given the large age uncertainties, we do not attempt to calculate the respective dynamical ages; however, we notice that  $T_{\text{cr}} \lesssim 10$  Myr for  $\sim 55$  per cent of the cases, suggesting that (even if their young ages are confirmed), a large fraction of the clumps we are observing can be of gravitationally bound systems.

## 5 DISCUSSION

### 5.1 Stellar clump populations

We discuss in this section, the results presented in Figs 5 and 6 and collected in Table 3 by putting the clump properties in the context of their host for each of the galaxies studied.

#### 5.1.1 The clump population of MS1358

MS1358 is characterized by the presence of several clumps; 10 were extracted in the western image (the one with the largest overall

**Table 3.** Main clump properties: (1) clump ID; (2) total magnification; (3) tangential magnification, reported only if used to derive the intrinsic size,  $R_{\text{eff}}$ ; (4) intrinsic effective radius; (5) intrinsic absolute UV magnitude; (6) SFR (UV-derived) surface density; (7) stellar mass; (8) age range of uncertainty; (9) range of uncertainty for the colour excess; (10) mass surface density; (11) crossing time, defined by equation (1).

ID	$\mu_{\text{tot}}$	$\mu_{\text{tan}}$	$R_{\text{eff}}$	Mag <sub>UV</sub>	$\log(\Sigma_{\text{SFR}_{\text{UV}}})$	$\log(M_{\star})$	Age	$E(B - V)$	$\log(\Sigma_{M_{\star}})$	$T_{\text{cr}}$
(1)	(2)	(3)	[pc]	[AB]	[ $M_{\odot} \text{ yr}^{-1} \text{ kpc}^{-2}$ ]	[ $M_{\odot}$ ]	[Myr]	[mag]	[ $M_{\odot} \text{ pc}^{-2}$ ]	[Myr]
MS1358										
W_1	7.9 <sup>+7.1</sup> <sub>-0.9</sub>	–	74 <sup>+9</sup> <sub>-34</sub>	-20.1 <sup>+1.0</sup> <sub>-0.1</sub>	2.1 <sup>+0.4</sup> <sub>-0.4</sub>	9.1 <sup>+1.1</sup> <sub>-1.1</sub>	1–300	0.0–0.4	4.6 <sup>+1.2</sup> <sub>-1.1</sub>	3 <sup>+1</sup> <sub>-3</sub>
W_2	16.7 <sup>+10.1</sup> <sub>-2.8</sub>	–	48 <sup>+6</sup> <sub>-15</sub>	-18.3 <sup>+0.7</sup> <sub>-0.2</sub>	1.8 <sup>+0.3</sup> <sub>-0.3</sub>	8.0 <sup>+0.4</sup> <sub>-0.8</sub>	1–13	0.2–0.4	3.8 <sup>+0.5</sup> <sub>-0.8</sub>	5 <sup>+2</sup> <sub>-4</sub>
W_3	8.1 <sup>+7.1</sup> <sub>-0.9</sub>	–	138 <sup>+39</sup> <sub>-71</sub>	-17.9 <sup>+1.0</sup> <sub>-0.2</sub>	0.7 <sup>+0.5</sup> <sub>-0.5</sub>	9.1 <sup>+0.4</sup> <sub>-1.4</sub>	1–300	0.0–0.4	4.0 <sup>+0.6</sup> <sub>-1.4</sub>	7 <sup>+4</sup> <sub>-7</sub>
W_4	9.3 <sup>+6.8</sup> <sub>-1.2</sub>	–	67 <sup>+11</sup> <sub>-27</sub>	-17.7 <sup>+0.8</sup> <sub>-0.1</sub>	1.3 <sup>+0.4</sup> <sub>-0.4</sub>	7.4 <sup>+0.5</sup> <sub>-0.9</sub>	1–12	0.1–0.3	2.9 <sup>+0.6</sup> <sub>-0.9</sub>	17 <sup>+7</sup> <sub>-17</sub>
W_5	12.8 <sup>+8.9</sup> <sub>-1.9</sub>	6.0	66 <sup>+19</sup> <sub>-49</sub>	-17.4 <sup>+0.8</sup> <sub>-0.2</sub>	1.2 <sup>+0.6</sup> <sub>-0.4</sub>	8.8 <sup>+0.3</sup> <sub>-1.3</sub>	2–300	0.0–0.4	4.4 <sup>+0.7</sup> <sub>-1.3</sub>	3 <sup>+2</sup> <sub>-3</sub>
W_6	18.8 <sup>+11.1</sup> <sub>-3.5</sub>	–	109 <sup>+37</sup> <sub>-48</sub>	-17.0 <sup>+0.7</sup> <sub>-0.2</sub>	0.6 <sup>+0.4</sup> <sub>-0.4</sub>	7.4 <sup>+0.9</sup> <sub>-1.1</sub>	1–100	0.0–0.4	2.5 <sup>+0.9</sup> <sub>-1.2</sub>	34 <sup>+23</sup> <sub>-34</sub>
W_7	11.4 <sup>+7.9</sup> <sub>-1.6</sub>	–	118 <sup>+26</sup> <sub>-48</sub>	-17.3 <sup>+0.8</sup> <sub>-0.2</sub>	0.6 <sup>+0.4</sup> <sub>-0.4</sub>	7.5 <sup>+0.3</sup> <sub>-0.8</sub>	1–9	0.2–0.3	2.5 <sup>+0.4</sup> <sub>-0.8</sub>	36 <sup>+15</sup> <sub>-24</sub>
W_8	10.5 <sup>+7.5</sup> <sub>-1.4</sub>	5.5	50 <sup>+45</sup> <sub>-50</sub>	-16.2 <sup>+0.8</sup> <sub>-0.2</sub>	0.9 <sup>+0.9</sup> <sub>-0.8</sub>	7.7 <sup>+0.6</sup> <sub>-1.0</sub>	1–90	0.0–0.5	3.5 <sup>+1.1</sup> <sub>-1.2</sub>	7 <sup>+10</sup> <sub>-7</sub>
W_9	9.6 <sup>+7.6</sup> <sub>-1.2</sub>	–	172 <sup>+54</sup> <sub>-87</sub>	-17.6 <sup>+0.9</sup> <sub>-0.3</sub>	0.4 <sup>+0.5</sup> <sub>-0.5</sub>	7.5 <sup>+1.3</sup> <sub>-1.1</sub>	1–200	0.0–0.4	2.2 <sup>+1.4</sup> <sub>-1.1</sub>	61 <sup>+37</sup> <sub>-61</sub>
W_10	10.0 <sup>+7.8</sup> <sub>-1.3</sub>	4.9	125 <sup>+62</sup> <sub>-114</sub>	-17.2 <sup>+0.9</sup> <sub>-0.2</sub>	0.5 <sup>+0.8</sup> <sub>-0.6</sub>	8.9 <sup>+0.7</sup> <sub>-1.5</sub>	1–400	0.0–0.6	4.0 <sup>+1.0</sup> <sub>-1.6</sub>	7 <sup>+6</sup> <sub>-7</sub>
E_1	4.2 <sup>+1.4</sup> <sub>-0.8</sub>	–	101 <sup>+18</sup> <sub>-23</sub>	-19.8 <sup>+0.4</sup> <sub>-0.2</sub>	1.8 <sup>+0.2</sup> <sub>-0.2</sub>	8.9 <sup>+0.9</sup> <sub>-0.6</sub>	1–200	0.0–0.4	4.1 <sup>+1.0</sup> <sub>-0.6</sub>	5 <sup>+2</sup> <sub>-5</sub>
E_2	10.8 <sup>+5.1</sup> <sub>-1.3</sub>	7.0	34 <sup>+9</sup> <sub>-18</sub>	-18.3 <sup>+0.5</sup> <sub>-0.1</sub>	2.1 <sup>+0.5</sup> <sub>-0.3</sub>	7.9 <sup>+0.5</sup> <sub>-0.7</sub>	1–14	0.2–0.4	4.1 <sup>+0.7</sup> <sub>-0.7</sub>	3 <sup>+2</sup> <sub>-3</sub>
E_4	7.3 <sup>+2.7</sup> <sub>-0.9</sub>	5.0	57 <sup>+31</sup> <sub>-36</sub>	-17.3 <sup>+0.4</sup> <sub>-0.2</sub>	1.3 <sup>+0.6</sup> <sub>-0.5</sub>	7.7 <sup>+0.4</sup> <sub>-0.6</sub>	1–11	0.2–0.4	3.4 <sup>+0.7</sup> <sub>-0.8</sub>	9 <sup>+8</sup> <sub>-9</sub>
E_5	7.2 <sup>+3.2</sup> <sub>-1.2</sub>	–	130 <sup>+37</sup> <sub>-46</sub>	-17.6 <sup>+0.5</sup> <sub>-0.2</sub>	0.7 <sup>+0.3</sup> <sub>-0.3</sub>	8.5 <sup>+0.3</sup> <sub>-1.0</sub>	4–100	0.0–0.3	3.5 <sup>+0.4</sup> <sub>-1.0</sub>	12 <sup>+7</sup> <sub>-8</sub>
E_6	12.7 <sup>+5.9</sup> <sub>-1.4</sub>	8.3	73 <sup>+38</sup> <sub>-50</sub>	-16.6 <sup>+0.5</sup> <sub>-0.2</sub>	0.8 <sup>+0.6</sup> <sub>-0.5</sub>	7.3 <sup>+0.9</sup> <sub>-0.7</sub>	1–100	0.0–0.4	2.8 <sup>+1.1</sup> <sub>-0.8</sub>	20 <sup>+17</sup> <sub>-20</sub>
E_7	7.8 <sup>+3.2</sup> <sub>-1.0</sub>	–	109 <sup>+33</sup> <sub>-39</sub>	-17.2 <sup>+0.5</sup> <sub>-0.2</sub>	0.7 <sup>+0.3</sup> <sub>-0.3</sub>	6.9 <sup>+0.7</sup> <sub>-0.7</sub>	1–13	0.0–0.3	2.0 <sup>+0.8</sup> <sub>-0.7</sub>	61 <sup>+35</sup> <sub>-61</sub>
E_9	5.4 <sup>+2.1</sup> <sub>-0.9</sub>	–	113 <sup>+48</sup> <sub>-52</sub>	-17.3 <sup>+0.5</sup> <sub>-0.3</sub>	0.7 <sup>+0.4</sup> <sub>-0.4</sub>	7.0 <sup>+1.8</sup> <sub>-0.6</sub>	1–100	0.0–0.3	2.1 <sup>+1.9</sup> <sub>-0.7</sub>	56 <sup>+40</sup> <sub>-56</sub>
E_10	6.1 <sup>+2.4</sup> <sub>-1.0</sub>	4.0	151 <sup>+109</sup> <sub>-122</sub>	-17.3 <sup>+0.5</sup> <sub>-0.3</sub>	0.4 <sup>+0.7</sup> <sub>-0.7</sub>	8.2 <sup>+0.8</sup> <sub>-0.7</sub>	1–200	0.0–0.5	3.0 <sup>+1.1</sup> <sub>-0.9</sub>	22 <sup>+25</sup> <sub>-22</sub>
N_1	3.6 <sup>+1.5</sup> <sub>-1.0</sub>	–	121 <sup>+22</sup> <sub>-29</sub>	-19.9 <sup>+0.5</sup> <sub>-0.3</sub>	1.7 <sup>+0.2</sup> <sub>-0.2</sub>	8.4 <sup>+1.4</sup> <sub>-1.0</sub>	1–100	0.0–0.4	3.4 <sup>+1.4</sup> <sub>-1.0</sub>	13 <sup>+7</sup> <sub>-13</sub>
RCS0224										
E_1	28.2 <sup>+19.4</sup> <sub>-2.7</sub>	16.7	16 <sup>+3</sup> <sub>-11</sub>	-17.9 <sup>+0.7</sup> <sub>-0.1</sub>	2.6 <sup>+0.6</sup> <sub>-0.3</sub>	7.5 <sup>+0.2</sup> <sub>-0.8</sub>	1–20	0.0–0.2	4.3 <sup>+0.6</sup> <sub>-0.9</sub>	2 <sup>+1</sup> <sub>-2</sub>
E_2	47.3 <sup>+55.2</sup> <sub>-8.0</sub>	27.1	17 <sup>+3</sup> <sub>-17</sub>	-16.3 <sup>+1.3</sup> <sub>-0.2</sub>	1.9 <sup>+0.9</sup> <sub>-0.5</sub>	7.2 <sup>+0.7</sup> <sub>-1.4</sub>	1–70	0.0–0.3	4.0 <sup>+1.1</sup> <sub>-1.4</sub>	3 <sup>+1</sup> <sub>-3</sub>
E_3	52.2 <sup>+63.4</sup> <sub>-12.0</sub>	29.5	25 <sup>+6</sup> <sub>-25</sub>	-16.6 <sup>+1.3</sup> <sub>-0.3</sub>	1.7 <sup>+0.9</sup> <sub>-0.6</sub>	6.6 <sup>+0.3</sup> <sub>-1.3</sub>	11–15	0.0–0.0	3.0 <sup>+0.9</sup> <sub>-1.3</sub>	10 <sup>+3</sup> <sub>-10</sub>
W_2	35.3 <sup>+10.4</sup> <sub>-6.8</sub>	19.7	< 9 <sup>+2</sup> <sub>-3</sub>	-16.4 <sup>+0.3</sup> <sub>-0.2</sub>	2.5 <sup>+0.3</sup> <sub>-0.2</sub>	7.4 <sup>+0.7</sup> <sub>-0.4</sub>	1–90	0.0–0.3	> 4.7 <sup>+0.8</sup> <sub>-0.5</sub>	< 1 <sup>+0</sup> <sub>-1</sub>
W_3	36.7 <sup>+10.6</sup> <sub>-8.1</sub>	20.3	24 <sup>+5</sup> <sub>-7</sub>	-16.7 <sup>+0.3</sup> <sub>-0.2</sub>	1.7 <sup>+0.3</sup> <sub>-0.2</sub>	6.3 <sup>+0.4</sup> <sub>-0.3</sub>	1–12	0.0–0.1	2.8 <sup>+0.5</sup> <sub>-0.4</sub>	12 <sup>+4</sup> <sub>-9</sub>
C_2,3	82.4 <sup>+21.9</sup> <sub>-25.7</sub>	44.8	6 <sup>+3</sup> <sub>-3</sub>	-16.0 <sup>+0.3</sup> <sub>-0.3</sub>	2.7 <sup>+0.4</sup> <sub>-0.4</sub>	7.0 <sup>+0.7</sup> <sub>-0.6</sub>	1–60	0.0–0.2	4.7 <sup>+0.8</sup> <sub>-0.8</sub>	1 <sup>+1</sup> <sub>-1</sub>
MACS0940										
SE_1	26.1 <sup>+0.8</sup> <sub>-19.6</sub>	14.3	46 <sup>+37</sup> <sub>-14</sub>	-17.0 <sup>+0.1</sup> <sub>-0.8</sub>	1.3 <sup>+0.4</sup> <sub>-0.7</sub>	7.1 <sup>+0.8</sup> <sub>-0.1</sub>	1–2	0.1–0.2	3.0 <sup>+0.9</sup> <sub>-0.7</sub>	13 <sup>+15</sup> <sub>-6</sub>
SE_2	25.3 <sup>+0.7</sup> <sub>-18.9</sub>	13.9	24 <sup>+18</sup> <sub>-1</sub>	-17.4 <sup>+0.0</sup> <sub>-0.8</sub>	2.0 <sup>+0.3</sup> <sub>-0.6</sub>	7.9 <sup>+0.9</sup> <sub>-0.5</sub>	3–90	0.0–0.3	4.3 <sup>+0.9</sup> <sub>-0.8</sub>	2 <sup>+2</sup> <sub>-2</sub>
SE_3	25.6 <sup>+0.7</sup> <sub>-19.1</sub>	14.0	< 14 <sup>+11</sup> <sub>-0</sub>	-17.6 <sup>+0.0</sup> <sub>-0.8</sub>	2.5 <sup>+0.3</sup> <sub>-0.6</sub>	7.5 <sup>+1.0</sup> <sub>-0.1</sub>	11–40	0.0–0.1	> 4.4 <sup>+0.7</sup> <sub>-0.7</sub>	< 2 <sup>+2</sup> <sub>-2</sub>
SE_4	25.6 <sup>+0.9</sup> <sub>-19.1</sub>	13.9	55 <sup>+41</sup> <sub>-2</sub>	-17.3 <sup>+0.0</sup> <sub>-0.8</sub>	1.2 <sup>+0.3</sup> <sub>-0.6</sub>	7.7 <sup>+0.8</sup> <sub>-0.5</sub>	11–40	0.0–0.1	3.5 <sup>+0.8</sup> <sub>-0.8</sub>	8 <sup>+10</sup> <sub>-1</sub>
SE_5	27.1 <sup>+0.8</sup> <sub>-20.5</sub>	14.5	< 14 <sup>+146</sup> <sub>-14</sub>	-15.3 <sup>+0.2</sup> <sub>-0.8</sub>	1.6 <sup>+0.9</sup> <sub>-0.2</sub>	–	–	–	–	–
SE_6	29.2 <sup>+1.0</sup> <sub>-22.5</sub>	15.4	< 14 <sup>+19</sup> <sub>-14</sub>	-14.8 <sup>+0.3</sup> <sub>-0.9</sub>	1.4 <sup>+0.9</sup> <sub>-1.2</sub>	6.2 <sup>+1.0</sup> <sub>-0.5</sub>	1–30	0.0–0.2	> 3.1 <sup>+1.3</sup> <sub>-1.3</sub>	< 6 <sup>+13</sup> <sub>-6</sub>
SE_7	33.5 <sup>+1.5</sup> <sub>-26.6</sub>	17.1	44 <sup>+45</sup> <sub>-29</sub>	-15.7 <sup>+0.2</sup> <sub>-0.9</sub>	0.8 <sup>+0.7</sup> <sub>-0.9</sub>	6.6 <sup>+0.9</sup> <sub>-0.4</sub>	1–15	0.0–0.2	2.5 <sup>+1.1</sup> <sub>-1.0</sub>	22 <sup>+35</sup> <sub>-22</sub>
SE_8	26.1 <sup>+0.9</sup> <sub>-19.6</sub>	14.1	49 <sup>+36</sup> <sub>-2</sub>	-16.3 <sup>+0.0</sup> <sub>-0.8</sub>	0.9 <sup>+0.3</sup> <sub>-0.7</sub>	–	–	–	–	–
SW_1	13.2 <sup>+15.7</sup> <sub>-2.7</sub>	–	127 <sup>+13</sup> <sub>-75</sub>	-17.9 <sup>+1.3</sup> <sub>-0.2</sub>	0.7 <sup>+0.5</sup> <sub>-0.5</sub>	7.4 <sup>+0.2</sup> <sub>-1.3</sub>	1–10	0.1–0.1	2.4 <sup>+0.6</sup> <sub>-1.3</sub>	44 <sup>+9</sup> <sub>-39</sub>
SW_2	14.0 <sup>+15.3</sup> <sub>-2.9</sub>	9.9	< 20 <sup>+4</sup> <sub>-20</sub>	-17.6 <sup>+1.2</sup> <sub>-0.2</sub>	2.2 <sup>+0.9</sup> <sub>-0.5</sub>	7.4 <sup>+0.2</sup> <sub>-1.2</sub>	3–13	0.1–0.2	> 4.0 <sup>+0.9</sup> <sub>-1.2</sub>	< 3 <sup>+1</sup> <sub>-3</sub>
SW_3	14.2 <sup>+13.3</sup> <sub>-3.0</sub>	10.0	39 <sup>+8</sup> <sub>-37</sub>	-18.2 <sup>+1.0</sup> <sub>-0.2</sub>	1.9 <sup>+0.8</sup> <sub>-0.4</sub>	8.1 <sup>+0.2</sup> <sub>-1.2</sub>	11–40	0.0–0.1	4.1 <sup>+0.8</sup> <sub>-1.2</sub>	3 <sup>+2</sup> <sub>-3</sub>
SW_4	13.8 <sup>+8.7</sup> <sub>-3.5</sub>	9.8	< 21 <sup>+12</sup> <sub>-17</sub>	-17.2 <sup>+0.7</sup> <sub>-0.3</sub>	2.0 <sup>+0.7</sup> <sub>-0.6</sub>	7.6 <sup>+0.3</sup> <sub>-0.7</sub>	1–11	0.2–0.3	> 4.2 <sup>+0.8</sup> <sub>-0.9</sub>	< 2 <sup>+2</sup> <sub>-2</sub>
SW_5,6	11.8 <sup>+2.4</sup> <sub>-4.1</sub>	8.4	29 <sup>+22</sup> <sub>-21</sub>	-16.4 <sup>+0.3</sup> <sub>-0.4</sub>	1.4 <sup>+0.7</sup> <sub>-0.7</sub>	7.2 <sup>+0.7</sup> <sub>-0.3</sub>	1–40	0.0–0.3	3.5 <sup>+1.0</sup> <sub>-0.8</sub>	6 <sup>+7</sup> <sub>-6</sub>
SW_7	11.6 <sup>+1.9</sup> <sub>-4.4</sub>	8.4	30 <sup>+38</sup> <sub>-30</sub>	-16.1 <sup>+0.3</sup> <sub>-0.5</sub>	1.3 <sup>+0.9</sup> <sub>-1.1</sub>	6.7 <sup>+0.9</sup> <sub>-0.4</sub>	1–30	0.0–0.2	3.0 <sup>+1.2</sup> <sub>-1.2</sub>	11 <sup>+21</sup> <sub>-11</sub>
N_9	12.8 <sup>+0.1</sup> <sub>-8.7</sub>	7.2	40 <sup>+42</sup> <sub>-32</sub>	-16.5 <sup>+0.1</sup> <sub>-0.7</sub>	1.2 <sup>+0.8</sup> <sub>-0.9</sub>	–	–	–	–	–
N_10	12.9 <sup>+0.2</sup> <sub>-8.7</sub>	7.2	110 <sup>+92</sup> <sub>-56</sub>	-16.4 <sup>+0.2</sup> <sub>-0.7</sub>	0.2 <sup>+0.5</sup> <sub>-0.7</sub>	–	–	–	–	–
N_11	12.5 <sup>+0.2</sup> <sub>-8.3</sub>	7.0	80 <sup>+72</sup> <sub>-49</sub>	-16.5 <sup>+0.2</sup> <sub>-0.7</sub>	0.5 <sup>+0.6</sup> <sub>-0.8</sub>	6.3 <sup>+0.7</sup> <sub>-0.1</sub>	1–10	0.0–0.0	1.7 <sup>+0.9</sup> <sub>-0.8</sub>	72 <sup>+99</sup> <sub>-70</sub>
E_9	6.5 <sup>+1.5</sup> <sub>-1.8</sub>	4.3	58 <sup>+122</sup> <sub>-58</sub>	-16.8 <sup>+0.3</sup> <sub>-0.4</sub>	1.0 <sup>+0.9</sup> <sub>-1.8</sub>	7.1 <sup>+0.7</sup> <sub>-0.3</sub>	1–50	0.0–0.2	2.8 <sup>+1.1</sup> <sub>-1.9</sub>	18 <sup>+58</sup> <sub>-18</sub>
E_10	5.8 <sup>+1.1</sup> <sub>-1.7</sub>	3.8	81 <sup>+24</sup> <sub>-15</sub>	-16.5 <sup>+0.2</sup> <sub>-0.3</sub>	0.6 <sup>+0.2</sup> <sub>-0.3</sub>	–	–	–	–	–
E_11	5.7 <sup>+1.0</sup> <sub>-1.7</sub>	–	197 <sup>+30</sup> <sub>-17</sub>	-17.5 <sup>+0.2</sup> <sub>-0.3</sub>	0.2 <sup>+0.2</sup> <sub>-0.2</sub>	–	–	–	–	–

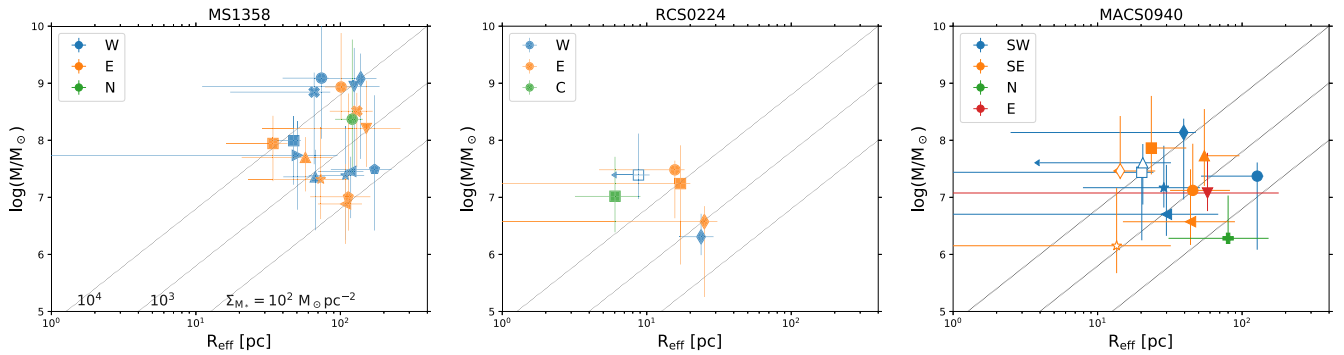


**Figure 6.** Intrinsic sizes and masses of the clumps. Solid grey lines are of constant mass surface density for  $10^2$ ,  $10^3$ , and  $10^4 M_{\odot} \text{pc}^{-2}$ . The same colour and marker notation as in Fig. 5 is used.

magnification), eight of which are also seen in the eastern image. The analyses on the two images of the galaxy produce comparable clump properties (see Table 3; Figs 5 and 6). For clump 8, visible only in the western part of the galaxy, we were not able to derive a robust size estimate. As suggested by previous studies and as clearly visible from Fig. 2, MS1358 is dominated in the rest-frame UV by two main clumps (ID: 1 and 2); those account for  $\sim 25$  per cent of the flux in  $F775W$ , rest-frame  $\sim 1300 \text{ \AA}$  (clump 1 alone accounts for  $\sim 20$  per cent, while if all clumps are considered, their contribution to the rest-frame UV emission of the galaxy is  $\sim 40$  per cent), suggesting that they are major contributors to the recent star formation of the galaxy. Their rest-frame UV fluxes, converted to the SFR via the Kennicutt & Evans (2012) relation, correspond to 5 and  $1 M_{\odot} \text{yr}^{-1}$ . Nebular tracers of the current star formation indicate that their contribution is even larger ( $\sim 40$  per cent of the SFR of the galaxy, Swinbank et al. 2009). The [O II]-derived SFR, 7.5 and  $3.7 M_{\odot} \text{yr}^{-1}$  for the two clumps<sup>7</sup>), suggests that the  $\text{SFR}_{\text{UV}}$  values we derived for our clumps may be underestimated; this could either be due to the SFR episode in the galaxy being more recent than what is assumed by the Kennicutt & Evans (2012) conversion and/or due to the presence of some extinction. The derived masses span the range  $10^7$ – $10^9 M_{\odot}$  and are therefore comparable to the mass of the entire galaxy as estimated by Swinbank et al. (2009). The derived young ages for some of the clumps ( $\lesssim 10$  Myr), combined to the nebular emission observed in the galaxy (Swinbank et al. 2009) suggest that a considerable fraction of the stellar mass in the galaxy is being formed during the current star formation episode, and that the clumps are an important contributor to that process.

### 5.1.2 The clump population of RCS0224

RCS0224 is characterized by three bright clumps, accounting for 45 per cent of the rest-frame UV emission. The brightest one (ID: 1,  $\text{SFR}_{\text{UV}} = 0.7 M_{\odot} \text{yr}^{-1}$ ) is not multiply imaged and therefore is only visible in the eastern image of the arc. The other two clumps do not have robust intrinsic size (and flux) estimates in the eastern image, due to the large uncertainties related to the magnification values; we can, however, rely on their properties derived in the western image. They are seen down to very small scales; both their sizes (below 10 pc for clump 2) and masses ( $10^6$ – $10^7 M_{\odot}$ ) are close to the ones of super star clusters in nearby galaxies (e.g. Leitherer et al. 2018;

Vanzella et al. 2019; Adamo et al. 2020b). The mass surface density of clump 3 ( $\Sigma_{M_*} \sim 10^3 M_{\odot} \text{pc}^{-2}$ ) is also consistent with nearby star clusters (e.g. Brown & Gnedin 2021), while clump 2 has a density close to  $\Sigma_{M_*} \sim 10^5 M_{\odot} \text{pc}^{-2}$ , one of the largest observed for star-forming regions (see also the discussion in Section 5.2). A single source is visible in the central image of the galaxy (see Fig. 3) but the lensing model cannot distinguish which source it is. The intrinsic size of the source is 6 pc and both the luminosity and mass suggest that this is another image of clump 2.

Summing the  $\text{SFR}_{\text{UV}}$  of the clumps in the central and western images and comparing it to the value estimated from [O II] emission in the same region ( $8.2 M_{\odot} \text{yr}^{-1}$ , Swinbank et al. 2007), we derive that only  $<10$  per cent of the galaxy SF is in the observed clumps. This result is consistent with bright [O II] emission being observed along the entire arc seen in  $F814W$  (a long part of which is devoid of compact sources, see Fig. 3); it may also indicate, as pointed out for MS1358, that  $\text{SFR}_{\text{UV}}$  values are underestimates and therefore that the bulk of star formation in the galaxy is very recent. This galaxy is also the one with the shallowest data (as discussed in Section 4.1), and therefore there is also the possibility that current observations are missing a population of low surface brightness clumps, currently undetected along the arc.

### 5.1.3 The clump population of MACS0940

Compact sources are seen all along the lensed arcs of MACS0940; the galaxy is dominated by four bright clumps (IDs: 1 to 4) contributing to  $\sim 40$  per cent of the rest-frame UV emission of the galaxy (the contribution of all the clumps in the arcs is  $\sim 50$  per cent). For some of the clumps, we were not able to derive robust size estimates. SE.5 and SE.6 have large size uncertainties; contrary to the rest of the sample, they both have de-lensed magnitudes that differ largely from their SW counterpart (SW.5, 6), hinting to a possible mis-association. We point out that there are no detected SW clumps with similar photometric properties to the former. Many of the clumps in the SW region (e.g. IDs: 2, 3, 4, and 7) also have large size uncertainties, mainly due to uncertainties in the lens model in that region of the arc; on the other hand, their SE counterparts have robust measurements that help inferring their intrinsic properties and will be used in the further analyses of this work, Section 5.2. For some clumps, we could not perform SED fitting due to the lack of signal in some of the filters (clumps SE.5, SE.7, N.10, N.11, E.11, and E.12). The sizes and masses of the bright clumps in the galaxy, distributed mainly between 15–60 pc and  $10^6$ – $10^8 M_{\odot}$ , lead to large-mass surface densities,  $\Sigma_{M_*} = 10^3$ – $10^4 M_{\odot} \text{pc}^{-2}$ . While little is

<sup>7</sup> Adapted from original values  $\text{SFR} = 12$  and  $6 M_{\odot} \text{yr}^{-1}$  reported in Swinbank et al. (2009), see footnote 2.



known about the properties of MACS0940, the clump contribution to the rest-frame UV emission and the spatial superposition of the peaks of Ly $\alpha$  emission (Claeysens et al. 2019) on the location of the brightest clumps suggest that the observed clumps are strongly contributing to the host galaxy recent star formation.

## 5.2 Comparison to literature samples

### 5.2.1 Size and SFR across redshifts

The sizes and luminosities of the clumps in these three galaxies are compared to samples from the literature in Fig. 7 (top-left-hand panel); in the case of clumps with multiple images, we will consider only the values recovered from the one with the highest magnification. The samples are colour-coded according to their redshift. The figure shows that, at any scale between  $\sim 1$  and  $\sim 10^3$  pc, clumps become on average increasingly brighter, moving to higher redshifts; a similar trend was already suggested by Livermore et al. (2015) using samples studied in H $\alpha$  emission. We point out that the SFR scale in Fig. 7 (derived from the Kennicutt & Evans 2012 conversion, as already described in Section 4.1), is used to directly compare samples studied in H $\alpha$  (SINGS, L12, L15, DYNAMO, see figure caption) to the others studied in rest-frame UV. We are not including, in this study, SFR values derived from the analysis of the clump spectral energy distributions.<sup>8</sup> The average clump SFR<sub>H $\alpha$</sub>  surface densities for  $z = 0, 1, 3,$  and  $5$  proposed by Livermore et al. (2015) are shown as dashed lines in Fig. 7 (top-left-hand panel), and are consistent with the overall densities of the plotted samples. In the same figure, we show as black–grey contours (enclosing 1 and  $2\sigma$  of the sample), the sizes and SFRs of H II regions in the SINGS sample of local MS galaxies (Kennicutt Robert C. et al. 2003); already at  $z = 1$ , clumps are clearly detached from the region covered by the SINGS sample, as pointed out by previous studies (e.g. Livermore et al. 2012a, 2015; Messa et al. 2022; Claeysens et al. 2023).

The redshift evolution of clump  $\Sigma_{\text{SFR}}$  is made explicit in the bottom-left-hand panel of Fig. 7 via violin distributions. For the whole sample, we consider only clumps with  $R_{\text{eff}} < 100$  pc, as we want to focus this analysis on compact star-forming regions; however, similar results would be derived considering clumps at all scales (see Appendix B). A clear redshift evolution of  $\Sigma_{\text{SFR}}$  is observed comparing local clumps ( $z = 0$ ) to samples at cosmic ‘afternoon’ ( $0 < z < 1.5$ ) and at cosmic noon ( $1.5 \leq z < 3.5$ ). A shallower evolution is seen at earlier cosmic times: while the distributions are on average shifted towards denser  $\Sigma_{\text{SFR}}$  at higher redshifts, extreme values can be observed already at  $z \sim 2$ , as it is the case for the clump population of the *Sunburst* galaxy (purple triangles in the top-left-hand panel of Fig. 7), studied at scales  $< 10$  pc (Vanzella et al. 2022b).

A necessary caveat is that the surface brightness completeness is different for each of the samples considered. Completeness limits are unavailable for many of the samples; however, it can be assumed that they become brighter moving to higher redshift. For example, the completeness limits derived in the current work,  $1\text{--}10 M_{\odot} \text{ yr}^{-1} \text{ kpc}^{-2}$ , are larger than the densest clumps at  $z < 1.5$ . We argue that the completeness limits, biasing the study of high- $z$  systems towards the most extreme (i.e. densest) sources, may be the main driver of the  $\Sigma_{\text{SFR}}$  redshift evolution overall, especially of the

median values of their distributions. As mentioned in the discussion of individual galaxies (Section 5.1), other factors possibly affecting the overall  $\Sigma_{\text{SFR}}$  distributions are the ages of the clumps and their extinctions. On the other hand, we expect that the high-density end of each distribution is not affected by the completeness; in this case, the evolution of the densest clumps would be real and may reflect the redshift evolution of the properties of their host galaxies. We also remind that there is a great in-homogeneity in how the considered literature samples were selected and analysed. Systematic statistical studies of clumps across redshift ranges are needed to truly prove and map the evolution of clumps; forthcoming studies with the *JWST* will indeed provide this statistics.

We can interpret the clump  $\Sigma_{\text{SFR}}$  redshift evolution discussed in this section as an evolution of the host galaxy conditions, where the clumps form. Main sequence galaxies are characterized by higher SFR densities at higher redshift, with the most extreme change happening during the cosmic noon ( $z = 1\text{--}3.5$ , e.g. Schreiber et al. 2015). In order to test this possibility, we consider in the next section, the properties of clumps in local starburst galaxies, i.e. galaxies which do not fall into the local main sequence but rather present typical properties of higher redshift systems.

### 5.2.2 Size and SFR of nearby samples

In order to test the effects of galaxy environments on their stellar clump population, we consider local samples of galaxies characterized by properties typical of high- $z$  systems. Galaxies in the DYNAMO sample, at  $z = 0.2$ , were selected to contain gas-rich galaxies with turbulent and marginally stable discs, well representing the star formation conditions at cosmic noon,  $z \sim 1\text{--}3$  (Green et al. 2014); their star-forming regions were studied in H $\alpha$  down to  $\sim 50$  pc resolution (Fisher et al. 2017a). In a similar way, the Lyman-Alpha Reference Sample (LARS), at redshift  $z = 0.03\text{--}0.20$ , contains galaxies selected to be analogues of  $z \sim 3$  (Lyman-break and Lyman-emitter) galaxies, characterized by elevated UV luminosities and SFRs (Östlin et al. 2014); their stellar clumps were studied in far-UV emission down to 10 pc scales (Messa et al. 2019). Finally, blue compact galaxies (BCGs) are (usually low mass) star-forming systems with high specific star formation rate (e.g. Östlin et al. 2001); among the best studied ones, SBS 0335–052E, ESO 338-IG04, and Haro 11 are known to host populations of bright young stellar clusters/clumps (e.g. Östlin & Kunth 2001; Östlin et al. 2003; Adamo et al. 2010; Adamo, Östlin & Zackrisson 2011; Sirressi et al. 2022). Sizes and UV magnitudes of clumps in ESO 338-IG04 were derived in Messa et al. (2019). No size measurements are available in the literature for clumps in SBS 0335–052E and Haro 11; we therefore perform, for the clumps in these galaxies, the same size-luminosity analysis described in Section 3.2 in the F140LP filter, tracing FUV emission.

The sizes, UV magnitudes (and SFRs), and  $\Sigma_{\text{SFR}}$  distributions of the clumps in these nearby samples are shown in Fig. 7 (top-right-hand and bottom-left-hand panels). In the case of SBS 0335–052E, we plot the six main *super star clusters* discussed in Adamo et al. (2010); for Haro 11 we select, from the sample of Sirressi et al. (2022), the brightest clusters, corresponding to UV magnitudes  $< 23$  mag; for ESO 338-IG04 and LARS, we plot all the clumps from the Messa et al. (2019) samples with a photometric uncertainty  $< 0.3$  mag in UV. Clump sizes span a broad range from 4 (individual stellar clusters) to  $\sim 1$  kpc (large star-forming regions). When considering only the compact ( $R_{\text{eff}} < 100$  pc) clumps in Fig. 7 (bottom-left), their median SFR surface densities are similar to the ones of clumps observed in galaxies at  $0 < z < 3.5$ ; the most extreme cases

<sup>8</sup>The published sample from Meštrić et al. (2022) includes SED-derived SFR values; however, for consistency with the other samples included in Fig. 7, we chose to plot only their rest-frame UV magnitudes.

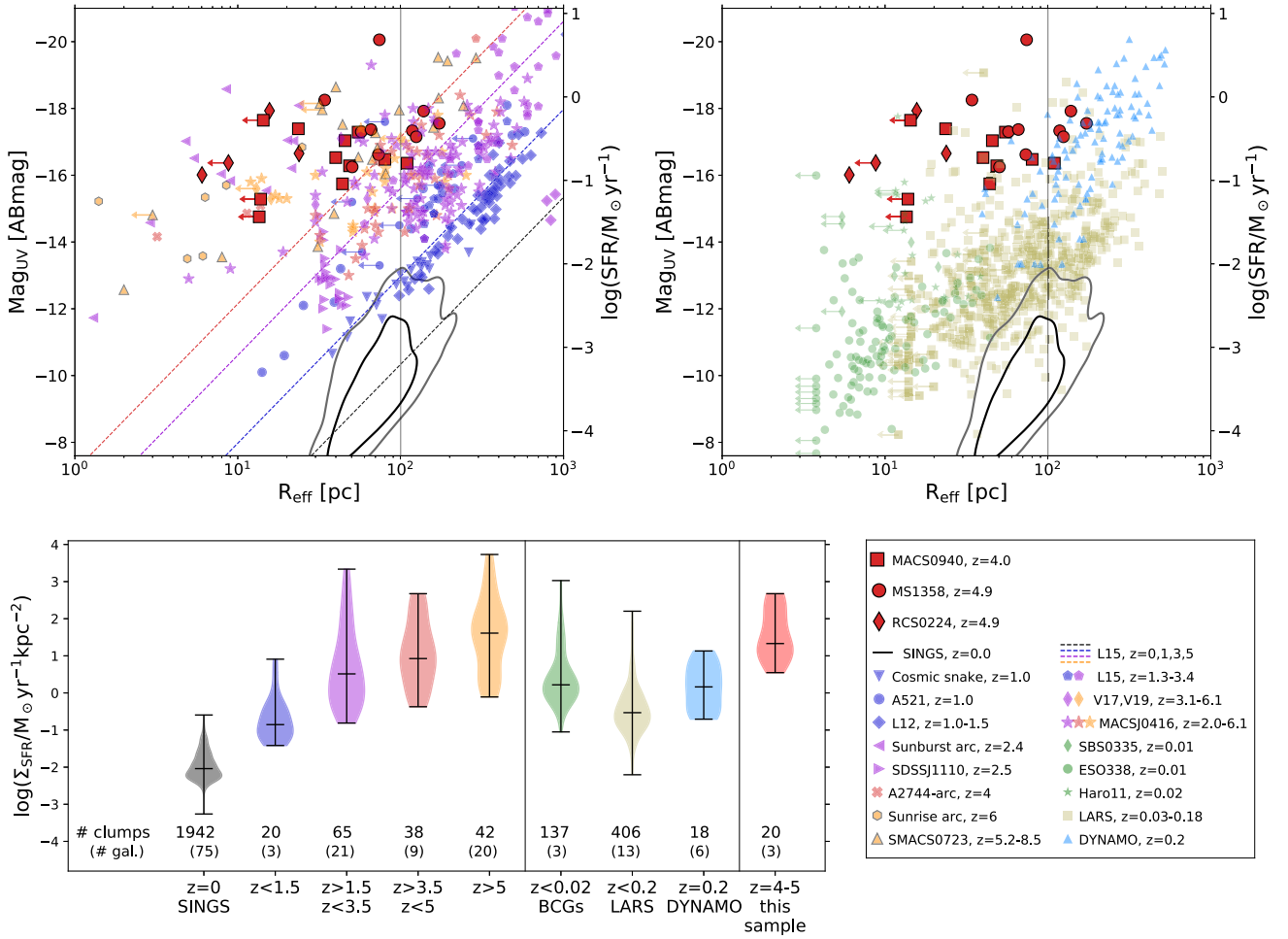


**Figure 7.** (*Top left*): sizes and magnitudes of the clumps in the current study compared to clump samples from literature, colour-coded by their redshift (blue:  $z < 1.5$ , purple:  $1.5 \leq z < 3.5$ , red:  $3.5 \leq z < 5$ , orange:  $z \geq 5$ ). The sample at  $z = 0$  from SINGS (Kennicutt Robert C. et al. 2003) is shown as black density contours (enclosing 1 and  $2\sigma$  of the distribution). On the y-axis, we are showing either  $H\alpha$  luminosities converted to SFR values (for L12 and L15) or UV magnitudes (for the rest of the samples). Values of typical SFR surface densities for samples at  $z = 0, 1, 3$ , and  $5$ , as derived by L15 are shown as dashed lines. Individual redshifts (or ranges) for each of the samples are given in the bottom-right-hand panel. The references for the samples considered are: the *Cosmic snake* arc (Cava et al. 2018), A521-sys1 (Messa et al. 2022), L12 Livermore et al. (2012a), the *Sunburst* arc (Vanzella et al. 2022b), SDSSJ1110+6459 (Johnson et al. 2017), Abell2744-arc (Vanzella et al. 2022c), the *Sunrise* arc (Vanzella et al. 2022a), SMACS0723 (considering only clumps at  $z > 5$ , i.e. where *JWST*-NIRCam traces their rest-frame UV emission, see Claeysens et al. 2023), L15 (Livermore et al. 2015), V17&V19 Vanzella et al. (2017a,b, 2019), MACSJ0416 (Meštrić et al. 2022). In the case of multiply-imaged clumps, we consider only the one with the largest magnification. (*Top right*): comparison to nearby clump samples of: blue compact galaxies (ESO338-IG04, Messa et al. 2019; SBS0335-052E and Haro11, this work), LARS (Messa et al. 2019), and DYNAMO (Fisher et al. 2017a). On the y-axis, we are showing  $H\alpha$  luminosities converted to SFR values for DYNAMO and UV magnitudes for the rest of the samples. (*Bottom left*): distribution of SFR densities (shown as violin plots, with median and extreme values of the distribution marked) of the clump samples, binned by redshift; only clumps with  $R_{\text{eff}} < 100$  pc are considered. The clumps from the current work are also shown as a separate panel.

are as dense as the clumps in the  $z \sim 5$  of the sample studied in this work. These distributions suggest that the environmental conditions setting the starburst nature of these galaxies (interactions, mergers, elevated gas fractions, and turbulence) can indeed drive the formation of clumps with elevated SFR densities.

### 5.2.3 Mass surface densities

We investigate if the SFR redshift evolution discussed in Section 5.2.1 (and Fig. 7) is also reflected in the clump masses. We plot in Fig. 8 the clump mass surface densities,  $\Sigma_{M_*}$ , as a function of the clump sizes (left-hand panel) and as violin distributions (right-hand panel); we use the same clump samples as in Fig. 7, when mass values are available. In more detail, masses are unavailable for L12, L15,

SDSSJ1110, the nearby DYNAMO sample, and the SINGS sample of local galaxies; instead, we plot the LEGUS sample of local clusters (from the analysis of Brown & Gnedin 2021) to help the comparison of compact clumps to single stellar clusters. For comparison, we provide also the stellar surface density of a typical  $10^{5.2} M_{\odot}$  globular cluster with  $R_{\text{eff}} = 3$  pc (Brodie & Strader 2006). In this analysis, we consider the entire SMACS0723 sample by Claeysens et al. (2023) and not only the one at  $z > 5$ , as done in Fig. 7, because the selection here is based on clump mass and not on FUV luminosity. The references for the samples are the same reported in the caption of Fig. 7, except for masses of clumps in: (i) SBS0335-052E, from Adamo et al. (2010); (ii) Haro 11, from Sirressi et al. (2022); (iii) ESO338-IG04 and LARS, from a forthcoming paper (Messa et al., in preparation).

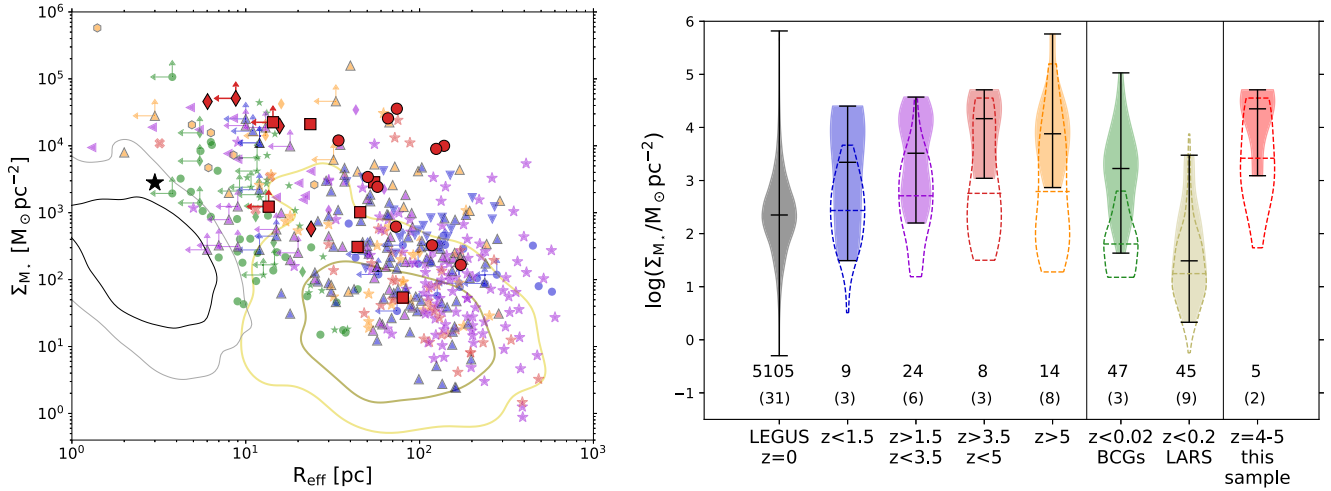


**Figure 8.** (*Left-hand panel*): mass surface densities of clumps in function of their intrinsic sizes; the colour and marker coding of the plotted samples are the same presented in Fig. 7; the only differences are the LARS sample, plotted as yellow contours instead of square markers, and the inclusion of the LEGUS sample of local stellar clusters (from the analysis of Brown & Gnedin 2021), instead of SINGS, as black contours, due to the lack of available masses for the latter. Both yellow and black contours enclose 1 and  $2\sigma$  of the relative distribution. The location of a typical globular cluster with  $M = 10^5 M_{\odot}$  and  $R_{\text{eff}} = 3$  pc (Brodie & Strader 2006) is shown with a black star marker. (*Right-hand panel*):  $\Sigma_{M_*}$  distributions, shown as violin plots; the distributions of clumps with  $R_{\text{eff}} \leq 20$  pc are shown as filled violins, while clumps in range  $20 < R_{\text{eff}} \leq 100$  pc are shown with empty violins with dashed edges (a dashed line marks also the median value of each distribution).

Mass surface densities span almost five orders of magnitudes ( $\Sigma_{M_*} \sim 10^0\text{--}10^5 M_{\odot} \text{pc}^{-2}$ ). Contrary to the  $\Sigma_{\text{SFR}}$  values (Fig. 7), no clear redshift trend is visible in the left-hand panel of Fig. 8. Some of the clumps in the current study, from MS1358 and MACS0940, stand out, together with other few  $z > 1.5$  sources, as very dense ( $\Sigma_{M_*} > 10^4 M_{\odot} \text{pc}^{-2}$ ), large (20–100 pc) clumps; these are the densities of the densest gravitationally bound local stellar systems (young and globular clusters), yet on much larger scales. The absence of a clear redshift evolution of  $\Sigma_{M_*}$  can also be deduced from redshift-binned violin distributions (see Appendix B).

A tentative redshift evolution of  $\Sigma_{M_*}$  can be seen when considering the clumps at  $R_{\text{eff}} \leq 20$  pc, i.e. at the scales of star clusters, Fig. 8, right-hand panel. An apparent feature of the figure is the increase in the upper-end of the  $\Sigma_{M_*}$  distribution at  $z > 5$ , but this is driven by a single massive ( $M \sim 10^7 M_{\odot}$ ) compact ( $R_{\text{eff}} = 1.4$  pc) source observed in the *Sunrise* arc (Vanzella et al. 2022a). The high-stellar densities of high- $z$  clumps become evident when local clusters are considered (black contours and black distribution in Fig. 8); there is only little overlap between local clusters and their counterparts at higher redshifts, the latter being on average denser. As already suggested in the previous section, this evolution probably reflects the ambient pressure where clusters form; galaxies at higher redshift are characterized by densest environment, which in turn are able to form denser clusters. This environmental effect was observed locally for stellar clusters (e.g. Johnson et al. 2017; Messa et al. 2018; Adamo et al. 2020b). This trend seems to be confirmed by the clumps in the local starburst BCGs, reaching densities comparable to their  $z > 1.5$  counterparts. We would like to point out that the current sample of high- $z$  clumps with  $R_{\text{eff}} \leq 20$  is very limited; new insight will come from samples observed with *JWST* able to combine extreme spatial resolution with a better age and mass characterization of the clumps (see, e.g. Claeysens et al. 2022; Vanzella et al. 2022a, c). We also notice that at larger scales ( $R_{\text{eff}} > 20$  pc, dashed violin distributions in Fig. 8) only clumps from the  $z > 1.5$  samples are observed to reach the most extreme densities ( $\Sigma_{M_*} \gtrsim 10^4 M_{\odot} \text{pc}^{-2}$ ), again suggesting a redshift evolution even for large star-forming complexes.

As final remark, we remind that UV luminosities, and consequently  $\text{SFR}_{\text{UV}}$  values, are strongly affected by the age and extinction of the clumps; this could be the cause of the different strengths in the redshift evolution of  $\Sigma_{M_*}$  and  $\Sigma_{\text{SFR}_{\text{UV}}}$ .

## 6 CONCLUSIONS

We presented the analysis of a small sample of stellar clumps in three galaxies at redshift between 4 and 5, namely the lensed arcs beyond the galaxy clusters MS1358, RCS0224, and MACS0940. These galaxies were chosen to be among the most highly magnified systems hosting multiple stellar clumps in a redshift range currently under-represented in clump studies. Each galaxy is multiply-imaged; many of the images are amplified by factors  $\mu > 5$  and reaching in some cases,  $\mu > 20$ . The clumps were studied using multiband photometry from the *HST*, providing a maximum angular resolution for the clump radii of  $\sim 0.02$  arcsec; combined to the large amplifications of these systems, it allows the study of physical scales down to  $\sim 10$  pc, i.e. comparable to the sizes of individual stellar clusters.

Clump populations in the three galaxies were extracted from a reference rest-frame UV filter (ACS-WFC-F775W for MS1358, ACS-WFC-F814W for RCS0224, and MACS0940); we further checked that our extraction did not miss clumps of different (redder) colours by testing the clump extraction also on the other available *HST* filters. Clump colours in combination with the lens models were used to recognize (and discard) foreground sources in the field; we find in total 10 unique clumps in MS1358, three in RCS0224 and 11 in MACS0940.

Clumps sizes and magnitudes were derived in the reference rest-frame UV filter for each of the galaxies; the other filters were used to fit a broad-band SEDs and derive the clump masses. Intrinsic sizes, magnitudes, and masses were derived using the lens models; due to the large amplifications involved, the uncertainties associated to the amplification factors dominate these intrinsic quantities. The derived effective radii range from  $\sim 10$  to  $\sim 200$  pc; the smallest sizes are reached in RCS0224, the galaxy with the largest amplification,



where we observe sources down to  $R_{\text{eff}} = 6$  pc. UV magnitudes are also converted to  $\text{SFR}_{\text{UV}}$  following the conversion by Kennicutt & Evans (2012); they range from  $\sim 10^{-2}$  to the most extreme values of  $5 M_{\odot} \text{ yr}^{-1}$  in MS1358. The completeness limits of the samples when converted into  $\text{SFR}_{\text{UV}}$  surface densities,  $\Sigma_{\text{SFR}}$ , are typically  $\sim 10 M_{\odot} \text{ yr}^{-1} \text{ kpc}^{-2}$ , and in all cases above  $1 M_{\odot} \text{ yr}^{-1} \text{ kpc}^{-2}$ , i.e. above the typical value for clumps in local main sequence galaxies (Kennicutt Robert C. et al. 2003; Livermore et al. 2015); we deduce that an eventual population of clumps with low surface brightness would be missed in this study.

By focusing individually on the galaxies of this study, we find that:

(i) the morphology of MS1358 is dominated by two bright clumps, accounting for 20 and 5 per cent of its rest-frame UV emission; when all the 10 observed clumps are considered together, this fraction raises to  $\sim 40$  per cent. The UV-derived SFR,  $\text{SFR}_{\text{UV}}$ , of the brightest clumps are lower than the literature values derived from nebular emission (Swinbank et al. 2009), suggesting either the presence of dust extinction or that the current star-formation episode is much younger than the assumption used in the Kennicutt & Evans (2012) FUV-to-SFR conversion. Clump masses range between  $10^7$  and  $10^9 M_{\odot}$ ; they are consistent with the entire galaxy mass as derived by Swinbank et al. (2009). We deduce that clumps in MS1358 are major contributors to the recent star formation episode(s) in the galaxy and to the build-up of its mass. The two main clumps of MS1358 are the UV-brightest among the galaxies studied in the current work and among all the compact ( $R_{\text{eff}} < 100$  pc) clumps known in literature. Despite most of the clumps in this galaxy having sizes in the range of 50–100 pc, their mass surface densities are comparable (and in many cases higher) to the ones of the densest local stellar clusters.

(ii) RCS0224 is characterized by three bright and compact clumps, accounting for  $\sim 45$  per cent of the rest-frame UV emission. The galaxy also shows a larger region of diffuse UV emission, appearing as a very elongated arc devoid of clumps, but actively forming stars, as derived from nebular [O II] emission by Swinbank et al. (2007); deeper observation would be needed to test the presence of low-surface brightness clumps along the arc. Despite RCS0224 has the shallowest data in the studied sample, its large magnification allows it to reach very small intrinsic scales; the clumps sizes and masses,  $R_{\text{eff}} = 6\text{--}25$  pc and  $M_{\star} = 10^6\text{--}10^{7.5} M_{\odot}$ , respectively, are close to the ones of the most massive stellar clusters in local galaxies. As is the case for clumps MS1358, also in RCS0224 the clump densities reach higher values than what typically observed in local samples.

(iii) Four bright clumps characterize the rest-frame UV morphology of the lensed arc MACS0940, accounting for  $\sim 40$  per cent of the emission, with other four sources contributing to another  $\sim 10$  per cent. Their derived intrinsic sizes ( $R_{\text{eff}} = 10\text{--}100$  pc) and masses ( $M_{\star} = 10^6\text{--}10^8 M_{\odot}$ ) suggest also for these clumps extreme stellar densities.

Finally, we compare the SFR and stellar mass surface densities of the clumps to the ones of known samples in the literature. We find overall an increase of  $\Sigma_{\text{SFR}}$  with redshift, particularly when comparing clumps in local main sequence galaxies to their counterparts at cosmic noon  $z \sim 1\text{--}3.5$ ; the evolution is less prominent at higher redshifts. A weaker evolution is suggested for  $\Sigma_{M_{\star}}$  (more evident for very compact sources,  $R_{\text{eff}} \leq 20$  pc). We can interpret the evolution of both clump quantities in the context of the evolution of the properties of their host galaxies; the latter, at higher redshifts, are characterized by increasingly denser environments, which produce denser galactic (and subgalactic) star-forming regions and, in turn, also denser stellar products. This interpretation is supported by the study of nearby starburst galaxies, whose clump properties resemble

high- $z$  samples more than the local average ones. With current data, we do not find any discontinuity in the redshift evolution of SFR and  $M_{\star}$  surface densities when considering redshift earlier than cosmic noon ( $z > 3.5$ ); this may imply that the clump formation conditions at  $z \sim 5$  are not different compared to later times. This result is in line with recent ALMA findings suggesting the presence of turbulent disc galaxies even at  $z > 5$  (Jones et al. 2021; Lelli et al. 2021; Rizzo et al. 2021; Herrera-Camus et al. 2022; Parlanti et al. 2023).

We remark that these redshift trends and relative interpretations are still tentative, for two main reasons. First, populations of clumps below  $\sim 100$  pc are still limited, leading to a small sample statistics when a binning in redshifts is considered. Second, the samples considered are in-homogeneous in how they have been extracted and analysed; this is true especially for what concerns SED-derived quantities, e.g. clump masses, ages, and extinctions. On going observations with the *JWST* will go in the direction of tackling both problems by observing large galaxy samples and extending the rest-frame optical coverage also to high-redshift sources.

## ACKNOWLEDGEMENTS

This research made use of Photutils, an Astropy package for detection and photometry of astronomical sources (Bradley et al. 2020). MM acknowledges the support of the Swedish Research Council, Vetenskapsrådet (internationell postdok grant 2019–00502) and the financial support through grant PRIN-MIUR 2020SKSTHZ. AA and AC acknowledge the support of the Swedish Research Council, Vetenskapsrådet (2021-05559).

## DATA AVAILABILITY

The *HST* data underlying this article are accessible from the Hubble Legacy Archive (HLA) at <https://hla.stsci.edu/> or through the MAST portal at <https://mast.stsci.edu/portal/Mashup/Clients/Mast/Portal.html>. Proposal IDs of the observations used: 9717 (PI: H. Ford) and 11591 (J. Kneib) for MS1358; 9135 (M. Gladders) and 14497 (R. Smit) for RCS0224; 11103 (H. Ebeling) and 15696 (D. Carton) for MACS0940. The derived data generated in this research will be shared on reasonable request to the corresponding author.

## REFERENCES

- Abraham R. G., van den Bergh S., Glazebrook K., Ellis R. S., Santiago B. X., Surma P., Griffiths R. E., 1996, *ApJS*, 107, 1  
 Adamo A., Zackrisson E., Östlin G., Hayes M., 2010, *ApJ*, 725, 1620  
 Adamo A., Östlin G., Zackrisson E., 2011, *MNRAS*, 417, 1904  
 Adamo A., Östlin G., Bastian N., Zackrisson E., Livermore R. C., Guaita L., 2013, *ApJ*, 766, 105  
 Adamo A. et al., 2020a, *Space Sci. Rev.*, 216, 69  
 Adamo A. et al., 2020b, *MNRAS*, 499, 3267  
 Bertin E., Arnouts S., 1996, *A&AS*, 117, 393  
 Bournaud F. et al., 2014, *ApJ*, 780, 57  
 Bradley L. et al., 2020, *astropy/photutils*: 1.0.0.  
 Brinchmann J. et al., 1998, *ApJ*, 499, 112  
 Brodie J. P., Strader J., 2006, *ARA&A*, 44, 193  
 Brown G., Gnedin O. Y., 2021, *MNRAS*, 508, 5935  
 Calzetti D., Armus L., Bohlin R. C., Kinney A. L., Koornneef J., Storchi-Bergmann T., 2000, *ApJ*, 533, 682  
 Cava A., Schaerer D., Richard J., Pérez-González P. G., Dessauges-Zavadsky M., Mayer L., Tamburello V., 2018, *Nat. Astron.*, 2, 76  
 Claeysens A. et al., 2019, *MNRAS*, 489, 5022  
 Claeysens A. et al., 2022, *A&A*, 666, A78  
 Claeysens A., Adamo A., Richard J., Mahler G., Messa M., Dessauges-Zavadsky M., 2023, *MNRAS*

- Coe D. et al., 2019, *ApJ*, 884, 85
- Cowie L. L., Hu E. M., Songaila A., 1995, *AJ*, 110, 1576
- Dessauges-Zavadsky M., Adamo A., 2018, *MNRAS*, 479, L118
- Dessauges-Zavadsky M., Schaerer D., Cava A., Mayer L., Tamburello V., 2017, *ApJ*, 836, L22
- Dessauges-Zavadsky M. et al., 2019, *Nat. Astron.*, 3, 1115
- Dessauges-Zavadsky M. et al., 2020, *A&A*, 643, A5
- Dessauges-Zavadsky M. et al., 2023, *MNRAS*, 519, 6222
- Ebeling H., Edge A. C., Mantz A., Barrett E., Henry J. P., Ma C. J., van Speybroeck L., 2010, *MNRAS*, 407, 83
- Elmegreen B. G., 2010, in de Grijs R., Lépine J. R. D., eds, Proc. IAU Symp. Vol. 266, Star Clusters: Basic Galactic Building Blocks Throughout Time and Space. p. 3 preprint (arXiv:0910.4638)
- Elmegreen B. G., Elmegreen D. M., 2006, *ApJ*, 650, 644
- Elmegreen D. M., Elmegreen B. G., Ravindranath S., Coe D. A., 2007, *ApJ*, 658, 763
- Elmegreen B. G., Elmegreen D. M., Tompkins B., Jenks L. G., 2017, *ApJ*, 847, 14
- Ferland G. J. et al., 2013, *RMxAA*, 49, 137
- Fisher D. B. et al., 2017a, *MNRAS*, 464, 491
- Fisher D. B. et al., 2017b, *ApJ*, 839, L5
- Förster Schreiber N. M. et al., 2009, *ApJ*, 706, 1364
- Förster Schreiber N. M., Shapley A. E., Erb D. K., Genzel R., Steidel C. C., Bouché N., Cresci G., Davies R., 2011a, *ApJ*, 731, 65
- Förster Schreiber N. M. et al., 2011b, *ApJ*, 739, 45
- Franx M., Illingworth G. D., Kelson D. D., van Dokkum P. G., Tran K.-V., 1997, *ApJ*, 486, L75
- Gaia Collaboration et al., 2018, *A&A*, 616, A1
- Gieles M., Portegies Zwart S. F., 2011, *MNRAS*, 410, L6
- Girard M. et al., 2018, *A&A*, 613, A72
- Gladders M. D., Yee H. K. C., Ellingson E., 2002, *AJ*, 123, 1
- Green A. W. et al., 2014, *MNRAS*, 437, 1070
- Guo Y., Gialavisco M., Ferguson H. C., Cassata P., Koekemoer A. M., 2012, *ApJ*, 757, 120
- Guszejnov D., Hopkins P. F., Grudić M. Y., 2018, *MNRAS*, 477, 5139
- Herrera-Camus R. et al., 2022, *A&A*, 665, L8
- Hoffmann S. L., Mack J., Avila R., Martlin C., Cohen Y., Bajaj V., 2021, in American Astronomical Society Meeting Abstracts. p. 216.02
- Hopkins P. F., Hernquist L., Cox T. J., Kereš D., 2008, *ApJS*, 175, 356
- Iani E., Caputi K. I., Rinaldi P., Kokorev V. I., 2022, *ApJ*, 940, L24
- Immeli A., Samland M., Gerhard O., Westera P., 2004, *A&A*, 413, 547
- Johnson T. L. et al., 2017, *ApJ*, 843, L21
- Jones G. C. et al., 2021, *MNRAS*, 507, 3540
- Jullo E., Kneib J. P., Limousin M., Elíasdóttir Á., Marshall P. J., Verdugo T., 2007, *New J. Phys.*, 9, 447
- Kennicutt R. C. Jr, 1998, *ARA&A*, 36, 189
- Kennicutt R. C., Evans N. J., 2012, *ARA&A*, 50, 531
- Kennicutt R. C. Jr et al., 2003, *PASP*, 115, 928
- Kroupa P., 2001, *MNRAS*, 322, 231
- Krumholz M. R., McKee C. F., Bland-Hawthorn J., 2019, *ARA&A*, 57, 227
- Leethochawalit N., Jones T. A., Ellis R. S., Stark D. P., Zitrin A., 2016, *ApJ*, 831, 152
- Leitherer C. et al., 1999, *ApJS*, 123, 3
- Leitherer C., Byler N., Lee J. C., Levesque E. M., 2018, *ApJ*, 865, 55
- Lelli F., Di Teodoro E. M., Fraternali F., Man A. W. S., Zhang Z.-Y., De Breuck C., Davis T. A., Maiolino R., 2021, *Science*, 371, 713
- Livermore R. C. et al., 2012a, *MNRAS*, 427, 688
- Livermore R. C. et al., 2012b, *ApJ*, 758, L35
- Livermore R. C. et al., 2015, *MNRAS*, 450, 1812
- Lotz J. M., Jonsson P., Cox T. J., Croton D., Primack J. R., Somerville R. S., Stewart K., 2011, *ApJ*, 742, 103
- Lotz J. M. et al., 2017, *ApJ*, 837, 97
- Ma X. et al., 2020, *MNRAS*, 493, 4315
- Mandelker N., Dekel A., Ceverino D., DeGraf C., Guo Y., Primack J., 2017, *MNRAS*, 464, 635
- Marchesini D., van Dokkum P. G., Förster Schreiber N. M., Franx M., Labbé I., Wuyts S., 2009, *ApJ*, 701, 1765
- Meng X., Gnedin O. Y., 2020, *MNRAS*, 494, 1263
- Messa M. et al., 2018, *MNRAS*, 477, 1683
- Messa M., Adamo A., Östlin G., Melinder J., Hayes M., Bridge J. S., Cannon J., 2019, *MNRAS*, 487, 4238
- Messa M., Dessauges-Zavadsky M., Richard J., Adamo A., Nagy D., Combes F., Mayer L., Ebeling H., 2022, *MNRAS*
- Meštrić U. et al., 2022, *MNRAS*, 516, 3532
- Mowla L. et al., 2022, *ApJ*, 937, L35
- Östlin G., Kunth D., 2001, *A&A*, 371, 429
- Östlin G., Amram P., Bergvall N., Masegosa J., Boulesteix J., Márquez I., 2001, *A&A*, 374, 800
- Östlin G., Zackrisson E., Bergvall N., Rönnback J., 2003, *A&A*, 408, 887
- Östlin G. et al., 2014, *ApJ*, 797, 11
- Parlanti E., Carniani S., Pallottini A., Cignoni M., Cresci G., Kohandel M., Mannucci F., Marconi A., 2023, *A&A*, 673, A153
- Planck Collaboration et al., 2014, *A&A*, 571, A16
- Postman M. et al., 2012, *ApJS*, 199, 25
- Puech M., 2010, *MNRAS*, 406, 535
- Renaud F., Romeo A. B., Agertz O., 2021, *MNRAS*, 508, 352
- Repp A., Ebeling H., Richard J., 2016, *MNRAS*, 457, 1399
- Reibero B. et al., 2017, *A&A*, 608, A16
- Richard J. et al., 2010, *MNRAS*, 404, 325
- Richard J. et al., 2014, *MNRAS*, 444, 268
- Richard J. et al., 2021, *A&A*, 646, A83
- Rizzo F., Vegetti S., Fraternali F., Stacey H. R., Powell D., 2021, *MNRAS*, 507, 3952
- Rodrigues M. et al., 2016, *A&A*, 590, A18
- Ryon J. E. et al., 2015, *MNRAS*, 452, 525
- Ryon J. E. et al., 2017, *ApJ*, 841, 92
- Salpeter E. E., 1955, *ApJ*, 121, 161
- Schreiber C. et al., 2015, *A&A*, 575, A74
- Shibuya T., Ouchi M., Kubo M., Harikane Y., 2016, *ApJ*, 821, 72
- Simons R. C. et al., 2017, *ApJ*, 843, 46
- Sirressi M. et al., 2022, *MNRAS*, 510, 4819
- Smit R., Swinbank A. M., Massey R., Richard J., Smail I., Kneib J. P., 2017, *MNRAS*, 467, 3306
- Somerville R. S., Lemson G., Kolatt T. S., Dekel A., 2000, *MNRAS*, 316, 479
- Soto E. et al., 2017, *ApJ*, 837, 6
- Stark D. P., Ellis R. S., Bunker A., Bundy K., Targett T., Benson A., Lacy M., 2009, *ApJ*, 697, 1493
- Straughn A. N. et al., 2015, *ApJ*, 814, 97
- Swinbank A. M., Bower R. G., Smith G. P., Wilman R. J., Smail I., Ellis R. S., Morris S. L., Kneib J. P., 2007, *MNRAS*, 376, 479
- Swinbank A. M. et al., 2009, *MNRAS*, 400, 1121
- Swinbank A. M. et al., 2017, *MNRAS*, 467, 3140
- Tamburello V., Mayer L., Shen S., Wadsley J., 2015, *MNRAS*, 453, 2490
- Treu T. et al., 2023, *ApJ*, 942, L28
- Turner O. J. et al., 2017, *MNRAS*, 471, 1280
- van den Bergh S., Abraham R. G., Ellis R. S., Tanvir N. R., Santiago B. X., Glazebrook K. G., 1996, *AJ*, 112, 359
- van Dokkelaar F., Agertz O., Renaud F., 2022, *MNRAS*, 512, 3806
- Vanzella E. et al., 2017a, *MNRAS*, 467, 4304
- Vanzella E. et al., 2017b, *ApJ*, 842, 47
- Vanzella E. et al., 2019, *MNRAS*, 483, 3618
- Vanzella E. et al., 2021, *A&A*, 646, A57
- Vanzella E. et al., 2022a, *ApJ*, 945, 53
- Vanzella E. et al., 2022b, *A&A*, 659, A2
- Vanzella E. et al., 2022c, *ApJ*, 940, L53
- Vázquez G. A., Leitherer C., 2005, *ApJ*, 621, 695
- Wisnioski E. et al., 2015, *ApJ*, 799, 209
- Zackrisson E., Rydberg C.-E., Schaerer D., Östlin G., Tuli M., 2011, *ApJ*, 740, 13
- Zanella A. et al., 2015, *Nature*, 521, 54
- Zanella A. et al., 2019, *MNRAS*, 489, 2792

**APPENDIX A: BEST-FIT MODELS**

We collect data, best-fit clump models, and fit residuals in the reference filter of each galaxy in Fig. A1.

**APPENDIX B: ADDITIONAL PLOTS**

The distributions of  $\Sigma_{\text{SFR}}$  across redshift bins, shown in Fig. 7, are expanded to include clumps of all sizes, loosening the constraint of  $R_{\text{eff}} \leq 100$  pc in Fig. B1 (left-hand panel). The main result reported in Section 5.2.1, i.e. the overall redshift evolution of the  $\Sigma_{\text{SFR}}$  distributions, up to redshifts  $z \sim 3.5$  is valid also in this case; the main difference when comparing Fig. B1 to Fig. 7 is

the presence of more low- $\Sigma_{\text{SFR}}$  systems, reflected in longer tails at the bottom of the violin distributions. These low-density clumps are consistent with being ‘large’ ( $R_{\text{eff}} > 100$  pc) star forming regions.

In a similar way to what is done for the  $\Sigma_{\text{SFR}}$  distributions, the right-hand panel of Fig. B1 shows violin distributions of  $\Sigma_{M_*}$ , binned by redshift ranges and including clumps of all sizes. As already pointed out in Section 5.2.3, no clear redshift evolution for the mass surface density is observed for the overall sample; a tentative evolution can be deduced when only the very small clumps, with sizes consistent with individual stellar clusters ( $R_{\text{eff}} < 20$  pc) are considered (right-hand panel of Fig. 8).



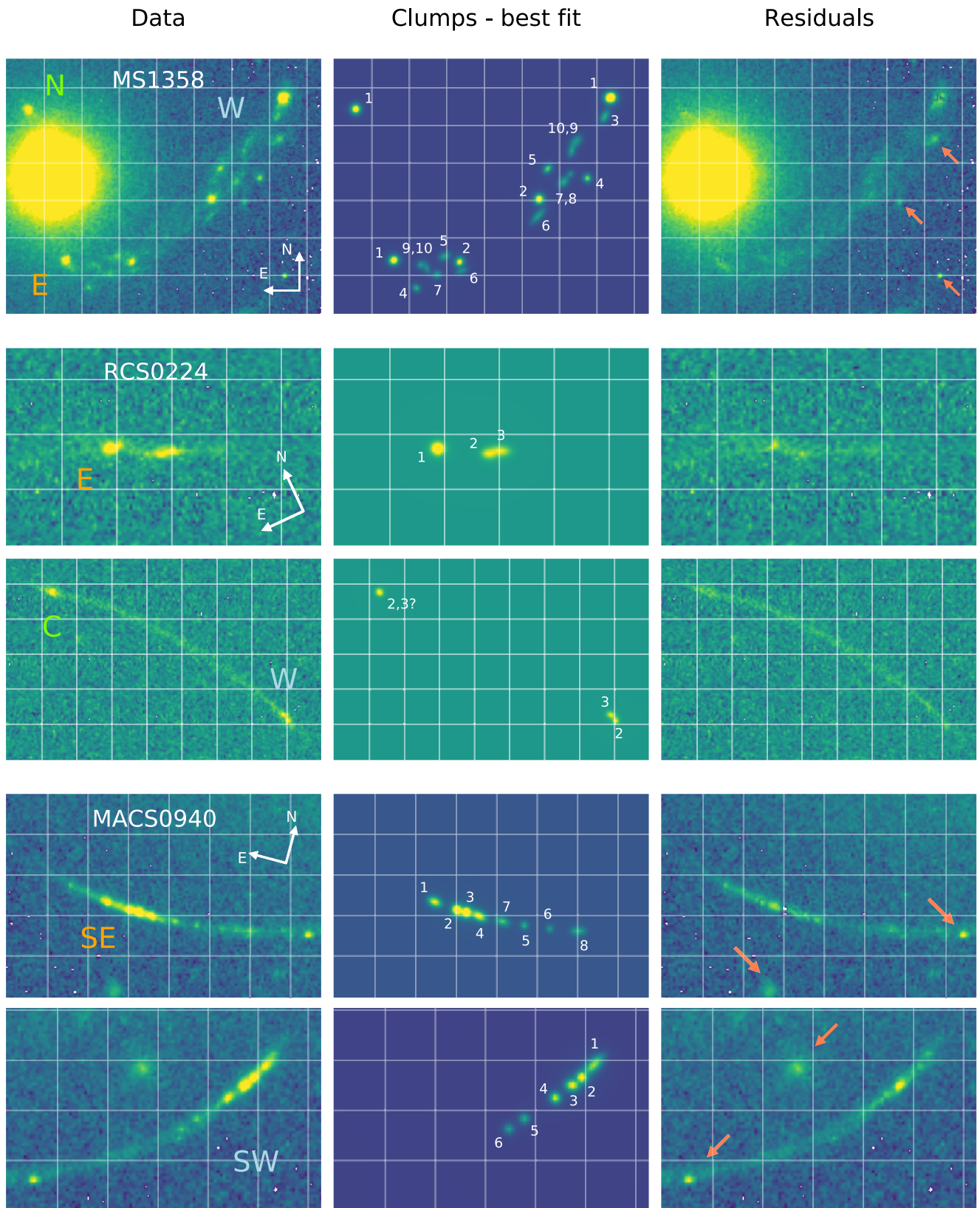


**Figure A1.** Data (left column), best-fit models (central column), and residuals (right column) for the main lensed arcs in the reference filters of each galaxy. Clumps IDs are reported in the central panels. Foreground sources are marked with red arrows in the right-hand panels. Grids of  $1 \times 1$  arcsec are plotted to facilitate the comparison between panels. For the position of the galaxy images within the cluster fields, see Figs 2, 3, and 4.

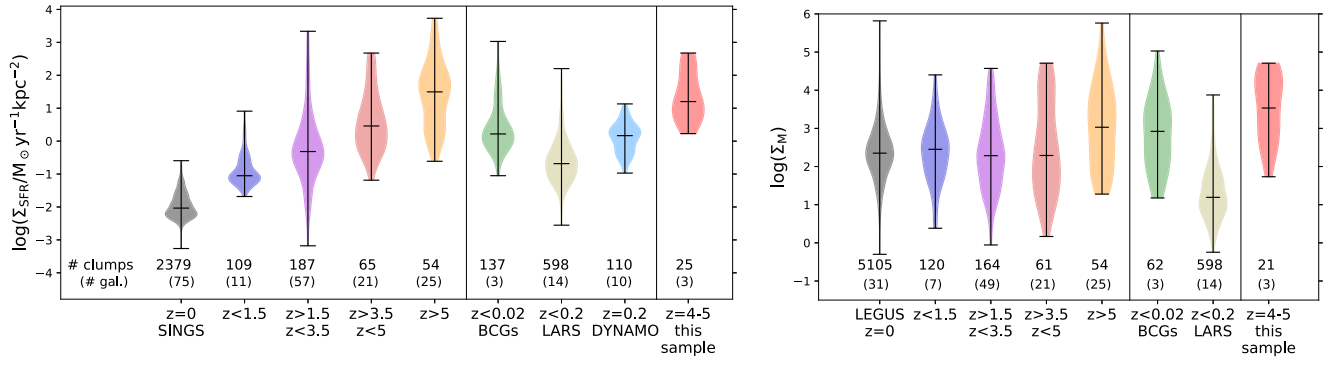


**Figure B1.** (Left): same as the bottom panel in Fig. 7, but including clumps of all sizes. (Right): same as the right-hand panel of Fig. 8 but including clumps of all sizes. The list and references of the samples used in both panels are given in the captions of Figs 7 and 8.

This paper has been typeset from a  $\text{\TeX}/\text{\LaTeX}$  file prepared by the author.